

# Low-Loss Inductor Design for High-Frequency Power Applications

by

Rachel S. Yang

S.B., Massachusetts Institute of Technology, 2018

Submitted to the  
Department of Electrical Engineering and Computer Science  
in Partial Fulfillment of the Requirements for the Degree of

Master of Engineering in Electrical Engineering and Computer Science

at the

Massachusetts Institute of Technology

June 2019

© 2019 Massachusetts Institute of Technology. All rights reserved.

Author:

---

Department of Electrical Engineering and Computer Science  
May 24, 2019

Certified by:

---

David J. Perreault  
Professor, Department of Electrical Engineering and Computer Science  
Thesis Supervisor

Accepted by:

---

Katrina LaCurts  
Chair, Master of Engineering Thesis Committee



# Low-Loss Inductor Design for High-Frequency Power Applications

by

Rachel S. Yang

Submitted to the Department of Electrical Engineering and Computer Science  
on May 24, 2019

in Partial Fulfillment of the Requirements for the Degree of  
Master of Engineering in Electrical Engineering and Computer Science

## Abstract

Miniaturization of power electronics can improve the performance of many applications, such as renewable energy systems, data centers, and aerospace systems. Operation in the high frequency (HF) regime (3–30 MHz) has potential for miniaturizing power electronics, but designing small, efficient inductors at HF can be challenging. At these frequencies, losses due to skin and proximity effects are difficult to reduce, and gaps needed to keep  $B$  fields low in the core add fringing field loss.

This thesis aims to improve the design of HF inductors. A low-loss inductor structure for HF applications and associated design guidelines that optimize for loss have been developed. The structure achieves low loss through quasi-distributed gaps and a new field shaping technique that achieves low winding loss through double-sided conduction. An example  $\sim 15\ \mu\text{H}$  inductor designed using the proposed guidelines achieved an experimental quality factor of 720 at 3 MHz and 2 A (peak) of ac current. In some cases, litz wire may further improve the performance of the proposed structure. With litz wire, the example inductor achieved an improved quality factor of 980.

The proposed structure also has great design and application flexibility. Core sets for this structure can be scaled by a factor-of-four in volume and still cover a large, continuous range of inductor requirements, e.g. power handling and inductances. A wide range of requirements can therefore be achieved with a small set of core pieces. The proposed inductor structure and design techniques thus have greater potential for commercial adoption to facilitate the design of low-loss HF inductors.

The design techniques used in the proposed structure can also be extended to high-power radio-frequency (RF) applications, such as RF power amplifiers for industrial plasma generation. A modified version of the proposed structure, along with modified design guidelines, can achieve low loss in this operating space. Simulations show that an example  $\sim 600\ \text{nH}$  inductor achieves a quality factor of 1900 at 13.56 MHz and 78 A (peak). Therefore, the developed design techniques and inductor structures are suitable for small, highly-efficient inductors at HF, and can thereby help realize high-frequency miniaturization of power electronics.

Thesis Supervisor: David J. Perreault

Title: Professor, Department of Electrical Engineering and Computer Science

## Acknowledgements

Thank you to Prof. David Perreault for the incredible opportunity to work on interesting research these past few years, and for your guidance and support.

Thank you to Prof. Charles Sullivan at Dartmouth for lending your expertise and guidance during the development of this work.

Thank you to Alex Hanson for your mentorship in everything, from technical skills to writing and presenting.

Thank you to Roderick Bayliss III for all your work on the high-power RF inductor.

The work relating to litz wire in Chapter 3 was carried out in close collaboration with Bradley Reese and Prof. Charles Sullivan from Dartmouth.

The ferrite core pieces for the prototypes in Chapter 3 were custom manufactured by Fair-Rite Products Corp. Thank you to Fair-Rite for taking the time and effort to do so.

# Contents

<b>1</b>	<b>Introduction</b>	<b>11</b>
<b>2</b>	<b>Proposed Low-Loss Inductor Structure and Design Guidelines</b>	<b>13</b>
2.1	Geometry Overview . . . . .	13
2.2	Design Guidelines . . . . .	13
2.2.1	Use quasi-distributed gaps to reduce gap fringing loss . . . . .	14
2.2.2	Balance $H$ fields to achieve multi-sided conduction . . . . .	15
2.2.3	Distribute $B$ fields to reduce overall core loss . . . . .	19
2.2.4	Select a wire size that optimizes effective conduction area . . . . .	19
2.2.5	Select a window size that balances gap fringing field loss and core loss in end caps to reduce overall loss . . . . .	20
2.2.6	Use a square aspect ratio to minimize overall loss . . . . .	21
2.2.7	Approximately balance copper and core loss to reduce overall loss . . . . .	21
2.3	Automating initial designs of the proposed structure . . . . .	22
<b>3</b>	<b>An Example 16.6 <math>\mu\text{H}</math> Design</b>	<b>25</b>
3.1	Simulation Results . . . . .	25
3.2	Experimental Results . . . . .	26
3.2.1	Experimental $Q$ measurements of the prototype verified simulations . . . . .	27
3.2.2	Prototype inductor achieves high $Q$ at higher frequencies . . . . .	27
3.2.3	Prototype inductor improved efficiency of a high-current-swing power converter . . . . .	28
3.3	Litz Wire in the Proposed Structure . . . . .	28
3.3.1	Design guidelines for optimizing litz wire . . . . .	29
3.3.2	Simulations showed litz wire improving $Q$ of prototype inductor at 3 MHz . . . . .	30
3.3.3	Experimental $Q$ measurements of litz wire prototype verified simulations . . . . .	31
3.3.4	Litz wire prototype can achieve high $Q$ at high frequencies . . . . .	32
<b>4</b>	<b>Design and Application Flexibility of the Proposed Structure</b>	<b>33</b>
4.1	Design Flexibility of a Single Core Set . . . . .	33
4.1.1	Inductance Range . . . . .	33
4.1.2	Power Handling Range . . . . .	35
4.2	Approaches for Covering a Wide Range of Inductor Requirements . . . . .	36
4.2.1	Factor-of-Two Volume Scaling . . . . .	36
4.2.2	Factor-of-Four Volume Scaling . . . . .	37

<b>5</b>	<b>Adapting the Proposed Structure for High-Power RF Applications</b>	<b>41</b>
5.1	Modified Geometry for High-Power RF Applications . . . . .	41
5.2	Changes in Design Guidelines . . . . .	42
5.2.1	Balance $H$ fields with the fringing field as the main flux return path to achieve double-sided conduction . . . . .	42
5.2.2	Select a wire size that balances effective conduction area and parasitic capacitance . .	44
5.2.3	Aim for a copper-loss dominated design for easier thermal management . . . . .	44
5.3	An Example 585 nH Design . . . . .	45
5.3.1	Simulation Results . . . . .	45
<b>6</b>	<b>Conclusion</b>	<b>47</b>
6.1	Key Takeaways . . . . .	47
6.2	Future Work . . . . .	47
<b>A</b>	<b>Designing the Distributed Gap Geometry to Minimize Gap Fringing Loss</b>	<b>49</b>
<b>B</b>	<b>Simulation Details for Chapter 2</b>	<b>50</b>
B.1	Simulation and Geometry Details for Fig. 2.3 . . . . .	50
B.2	Simulation and Geometry Details for Fig. 2.5 . . . . .	50
B.3	Simulation and Geometry Details for Table 2.1 . . . . .	51
B.4	Simulation and Geometry Details for Fig. 2.7 . . . . .	51
B.5	Simulation and Geometry Details for Fig. 2.9 . . . . .	52
B.6	Simulation and Geometry Details for Fig. 2.10 . . . . .	53
<b>C</b>	<b>First-Order Derivation of Loss in the Active Section</b>	<b>55</b>
<b>D</b>	<b>Example Python Script for Automating Initial Designs of the Proposed Structure</b>	<b>56</b>
<b>E</b>	<b>Prototype Construction</b>	<b>58</b>
E.1	Prototype Construction of the Example 16.6 $\mu$ H Design . . . . .	58
E.2	CAD Drawings for the Manufactured Core Pieces . . . . .	60
E.3	CAD Drawings for the 3D-printed Fixtures . . . . .	63
<b>F</b>	<b>Measuring High <math>Q</math> (large-signal)</b>	<b>65</b>
F.1	Use a capacitor divider to minimize probe loss and loading . . . . .	65
F.2	Include capacitor ESR to accurately measure high $Q$ . . . . .	66
F.3	Minimize dielectric loss through careful board layout . . . . .	67
F.4	Resonant measurement approach validated using an air-core inductor . . . . .	67
<b>G</b>	<b>Constant Heat Flux Model</b>	<b>68</b>
<b>H</b>	<b>Including Loss from Self-Resonant Circulating Currents in the Quality Factor</b>	<b>69</b>
<b>I</b>	<b>Example Python Script for Automating Initial Designs of the Modified Structure</b>	<b>70</b>
	<b>Bibliography</b>	<b>72</b>

# List of Figures

2.1	Radial cross-sectional view and 3D model of the proposed structure . . . . .	14
2.2	Important parameters of quasi-distributed gaps . . . . .	15
2.3	Single-sided versus double-sided conduction . . . . .	16
2.4	Magnetic circuit model used to balance the $H$ fields in the proposed structure . . . . .	16
2.5	Similar fringing fields of a solenoid and the proposed inductor . . . . .	17
2.6	Reproduced plot of the experimental quantity $F$ from [1] . . . . .	18
2.7	Optimal range of vertical window fill $F_v$ . . . . .	20
2.8	Flux crowding at the end of the window . . . . .	20
2.9	Optimal range of horizontal window fill $F_h$ . . . . .	21
2.10	Optimal aspect ratio . . . . .	22
2.11	Flowchart of the design process for the proposed inductor structure . . . . .	23
3.1	Simulations of the example 16.6 $\mu\text{H}$ design . . . . .	26
3.2	Prototype inductor of the example 16.6 $\mu\text{H}$ design . . . . .	27
3.3	Experimental $Q$ measurements of the prototype inductor . . . . .	27
3.4	$Q$ of prototype inductor across frequency . . . . .	28
3.5	Efficiencies of a power converter using the prototype inductor versus a conventional inductor design . . . . .	29
3.6	Thermal images of the prototype inductor versus a conventional inductor design . . . . .	29
3.7	Idealized cross-sections of litz wires with 450 strands using cabling and bunching twisting operations . . . . .	30
3.8	Simulated inductor $Q$ versus number of AWG 48 litz wire strands using a simple design method and FEA simulations of specific litz configurations at 3 MHz and 2 A (peak, ac) . . . . .	31
3.9	Experimental results of the prototype inductor using solid-core versus litz wire . . . . .	32
4.1	Core set with three types of magnetic parts . . . . .	34
4.2	Maximum power handling curve at $\Delta T = 40^\circ\text{C}$ of the MP27 core set at $h/D = 1$ . . . . .	35
4.3	Maximum power handling curves at $\Delta T = 40^\circ\text{C}$ of the MP27 core set at various aspect ratios . . . . .	36
4.4	Maximum power handling curves at $\Delta T = 40^\circ\text{C}$ of the MP27 and MP33 core sets at various aspect ratios . . . . .	37
4.5	Maximum power handling curves at $\Delta T = 40^\circ\text{C}$ of the MP27 and MP42 core sets at various aspect ratios . . . . .	38
4.6	Maximum power handling curves at $\Delta T = 40^\circ\text{C}$ of the MP17 and MP27 core sets at various aspect ratios . . . . .	38

4.7	Maximum power handling curves at $\Delta T = 40^\circ\text{C}$ of the MP17 and MP27 core sets outside the overlap region . . . . .	39
5.1	Radial cross-sectional view and 3D model of the modified proposed structure . . . . .	42
5.2	Magnetic circuit model used to balance the $H$ fields in the modified proposed structure . . .	43
5.3	$B$ field and $B$ field line simulations of the example 585 nH design . . . . .	46
5.4	Current distribution simulations of the example 585 nH design . . . . .	46
E.1	Construction of the prototype inductor using custom 3D-printed fixtures . . . . .	59
E.2	CAD drawing of the manufactured end cap part . . . . .	60
E.3	CAD drawing of the manufactured core disc part for the center post . . . . .	61
E.4	CAD drawing of the manufactured outer shell section . . . . .	62
E.5	CAD drawing of the custom 3D-printed fixture for the winding . . . . .	63
E.6	CAD drawing of the custom 3D-printed fixture for assembling the outer shell sections . . . .	64
F.1	Circuit for the modified resonant measurement approach to measure high $Q$ . . . . .	65
F.2	Thermal image showing a mica capacitor with a $\sim 13^\circ\text{C}$ temperature rise due to its ESR loss, in accordance with calculations . . . . .	66
H.1	Circuit for including loss from self-resonant circulating currents in the $Q$ of an inductor . . .	69



# List of Tables

2.1	Error of inductance model (Section 2.2.2) for 16.6 $\mu\text{H}$ designs . . . . .	19
3.1	Specifications for the simulated example inductor . . . . .	25
3.2	Geometry of the simulated example inductor . . . . .	25
3.3	The simulated example inductor and the prototype with 20 AWG wire . . . . .	26
3.4	Specifications for the conventional inductor . . . . .	28
3.5	The simulated example inductor and the experimental prototype with 5/9/10/48 litz wire . . . . .	31
4.1	Geometry of the MP17, MP27, MP33, and MP42 Core Sets . . . . .	37
5.1	Specifications for the simulated example RF inductor . . . . .	45
5.2	Geometry of the simulated example RF inductor . . . . .	45
B.1	Geometry of the simulated rod-core inductors in Fig. 2.3 . . . . .	50
B.2	Geometry of the simulated solenoid in Fig. 2.5 . . . . .	51
B.3	Geometry of the simulated inductors in Table 2.1 . . . . .	51
B.4	Core geometry for the simulations in Fig. 2.7 at different window heights $l_t$ . . . . .	51
B.5	Wire diameters for a range of vertical window fills at different window heights . . . . .	52
B.6	Core geometry for the simulations in Fig. 2.9 at different window widths . . . . .	52
B.7	Combinations of wire diameters $D_w$ and window widths $w$ to achieve a range of horizontal window fills $F_h$ at different vertical window fills $F_v$ . . . . .	52
B.8	Geometries for simulated inductors with different aspect ratios at a volume of 7 $\text{cm}^3$ from Fig. 2.10 . . . . .	53
B.9	Geometries for simulated inductors with different aspect ratios at a volume of 14 $\text{cm}^3$ from Fig. 2.10 . . . . .	54
B.10	Geometries for simulated inductors with different aspect ratios at a volume of 28 $\text{cm}^3$ from Fig. 2.10 . . . . .	54



# Chapter 1

## Introduction

Power electronics set the performance, size, and cost of many applications, including cost-effective renewable energy systems, efficient data centers, and light-weight aerospace systems. Miniaturizing power electronics can therefore advance these applications, as well as enable new applications where power electronics can be leveraged, such as the electrification of aircraft. At high-frequency operation (HF: 3–30 MHz), miniaturization and improved performance of power electronics is possible, but magnetic components, such as inductors and transformers, limit these advances. These components are often the largest and lossiest elements in power electronics, and making these components small and efficient at HF is particularly challenging due to losses in the core and winding [2].

Skin and proximity effects increase winding loss<sup>1</sup> of magnetic components and play a large role in the performance of magnetic components at HF. Skin effect causes current to flow near the surface of the conductor, rather than through the entire available cross-sectional area, thus increasing the effective resistance of the winding. The effective conductor area for current flow is characterized by the *skin depth*, which decreases with frequency. Proximity effect losses occur when high-frequency magnetic fields from nearby conductors induce eddy currents in a conductor. Having many layers of conductors thus increases proximity effect losses.

Conductors with diameters smaller than a skin depth reduce skin and proximity effect losses. Litz wire, which is composed of many strands of small-diameter wire twisted together in a specific fashion, is often used with strands thinner than a skin depth to reduce winding loss. At HF, though, conventional solutions for reducing winding loss, such as litz wire, become less practical due to manufacturing difficulties [3]. Therefore, other approaches for reducing proximity effect, such as single-layer windings or multi-layer foil windings, have been investigated [3–6].

Magnetic material properties, such as magnetic hysteresis and bulk conductivity, fundamentally lead to increased core loss with increased frequency, and core loss becomes an extremely important design factor at HF and above. Core loss also increases with  $B$  fields, so gaps are used to keep  $B$  fields low. At HF, gaps become particularly important to achieve low core loss.

Typically, gaps are implemented as a single lumped gap in the core. Fringing fields from the gap, though, cause current in the winding to crowd near the gap, significantly increasing winding loss. Various winding configurations and materials have been explored to deal with these effects [3, 7, 8]. In particular, distributed or quasi-distributed gaps have successfully mitigated fringing field effects [9] and are beginning to be implemented in cores on the market [10].

Recent development of high-performance core materials at HF has opened opportunities for improv-

---

<sup>1</sup>This thesis uses winding loss and copper loss interchangeably.

ing magnetics design. Many of these materials, however, have lower magnetic permeability compared to traditional materials, thus greatly changing design constraints and tradeoffs [11, 12].

To better understand the design challenges for magnetic components at HF, much research has focused on modeling. Analytical models of conductor loss [13–18] and core loss [19, 20] have been developed, with some work targeting the HF range [21]. While modeling can provide valuable analysis tools, development of HF magnetic structures and design guidelines is an additional important step.

This thesis aims to improve the design of HF inductors by exploring design methods for low core and winding losses at HF and by investigating approaches that use these methods to realize designs for a wide range of application requirements. Chapter 2 proposes a low-loss inductor structure suitable for HF applications with large ac currents and associated analytic design guidelines that maximize its quality factor<sup>2</sup>. The structure achieves high  $Q$  through quasi-distributed gaps and a new field shaping technique for low winding loss.

Chapter 3 presents an example 16.6  $\mu\text{H}$  inductor design of the proposed structure, which was designed using a largely automated process generated from the design guidelines. The example design was confirmed to achieve high  $Q$  at 3 MHz and 2 A (peak) of ac current through both simulation and experimental results, thus verifying that the design guidelines achieve low loss. This chapter also discusses using litz wire in the proposed structure to reduce loss, and additional guidelines for litz are included. Litz wire was demonstrated to further reduce loss in the example design.

Chapter 4 evaluates the performance and limitations of the structure across a range of inductor requirements. Approaches for using the proposed structure to cover a wide range of requirements with a small set of components are presented, with the goal of facilitating commercial adoption of the proposed structure and design techniques.

Chapter 5 extends the developed low-loss design techniques from Chapter 2 to high-power RF applications. Challenges in this operating space are discussed, and a modified structure and associated design guidelines are presented. An example 590 nH inductor is then designed using these modifications; this inductor design is suitable for use in high-power RF amplifiers and matching networks for industrial plasma drive. Simulations of the example design at 13.56 MHz and 78 A (peak) show that the developed design techniques can achieve high  $Q$  at higher power and frequency.

Chapter 6 summarizes key takeaways from this thesis and discusses future work.

---

<sup>2</sup>This thesis uses the following definition of inductor quality factor:  $Q = \omega L/R_{ESR}$ , where  $R_{ESR}$  is the equivalent series resistance of the inductor at the frequency of interest. Note that this definition provides a value that is equal to  $2\pi(\text{peak energy stored})/(\text{energy dissipated in a cycle})$  for a sinusoidal drive at the frequency of interest.

## Chapter 2

# Proposed Low-Loss Inductor Structure and Design Guidelines

This chapter proposes a low-loss inductor structure and associated design guidelines suitable for HF applications with large ac currents.<sup>1</sup> The structure uses quasi-distributed gaps and a new field shaping technique to achieve low loss. This chapter also presents analytic design guidelines that roughly maximize the  $Q$  of the proposed structure. These guidelines can then be largely automated to quickly generate initial designs, thus facilitating the design of low-loss HF inductors.

### 2.1 Geometry Overview

The proposed structure resembles a pot core, but has a specific geometry with a single-layer winding and quasi-distributed gaps in the center post and outer shell (Fig. 2.1). To implement the quasi-distributed gaps, the core is composed of thin magnetically permeable discs and outer shell sections separated by small gaps. The center post and outer shell are bridged by magnetic end caps at the top and bottom of the structure. A single-layer winding is centered in the window, with evenly spaced turns.

The permeable return path helps to contain the magnetic flux, increases achievable inductance, and improves the predictability of the inductance. The winding is kept to a single layer to reduce proximity-effect losses. The quasi-distributed gaps help reduce fringing field effects by distributing the MMF drops (and associated fields) in the vicinity of the conductors, while still allowing the use of a magnetic core material. When properly designed, the structure uses a new approach of field shaping to reduce winding loss by more effectively using the available winding area for conduction; this crucial benefit is described in detail in Section 2.2.2.

### 2.2 Design Guidelines

The design guidelines below optimize the  $Q$  of the proposed structure at a given volume and inductance for applications where ac losses dominate. Most of the guidelines can be mathematically defined so that initial designs can be largely automated. A few of the parameters, however, must be manually tuned using the guidelines, as would be done in a non-analytic design process. Slight deviation from the optimized

---

<sup>1</sup>Chapters 2 and 3 are adapted from the author's publications [22, 23].

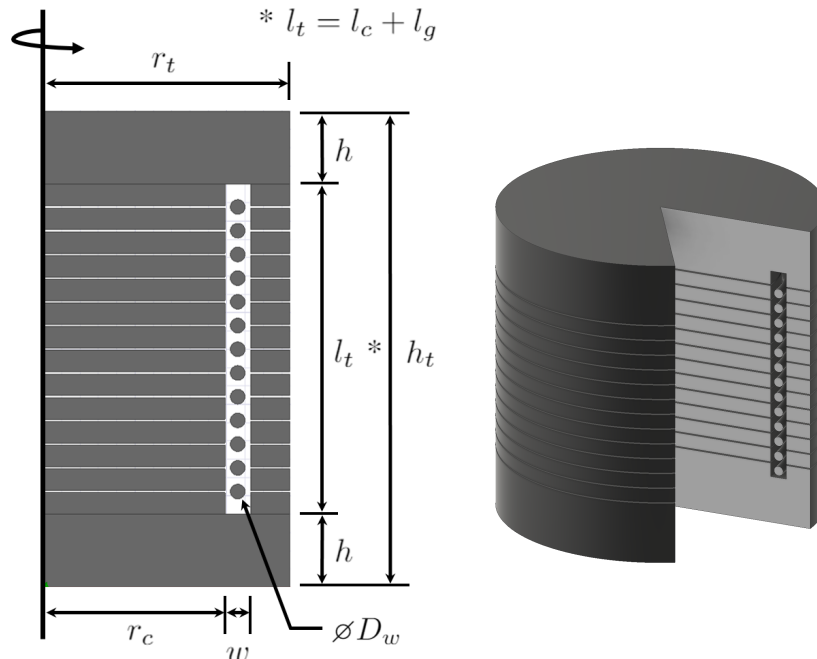


Figure 2.1: Radial cross-sectional view (left) of the proposed inductor, with a center post, outer shell, and end caps encasing a single-layer winding. Parameters defining the geometry are labelled on this view as reference for Section 2.3. Revolving the cross-section about the axis of rotation produces the 3D model of the inductor on the right (a piece is cut out for clarity).

parameters, e.g. due to manufacturing tolerances, minimally impacts the  $Q$  of the structure, as the trade-off for each parameter falls off slowly near the optimum.<sup>2</sup>

### 2.2.1 Use quasi-distributed gaps to reduce gap fringing loss

Gapping ferrite cores in high-current-swing applications is important for keeping  $B$  fields low to reduce core loss, which scales as  $B^\beta$  (for high-frequency ferrites,  $\beta \approx 2-3$ ), per the Steinmetz equation  $P_v = k_c f^\alpha B^\beta$  [24, 25]. As frequency increases, ever lower  $B$  fields are needed to keep core loss low, leading to larger gaps. The impact of fringing fields from gaps on copper losses can thereby become more severe at higher frequencies. To reduce the fringing loss, the proposed inductor uses quasi-distributed gaps [9], as opposed to a conventional single lumped gap. Instead of dropping the entire MMF across one gap, the quasi-distributed gap has a smaller MMF drop across each of multiple gaps, causing less total loss in the winding. As shown in [9], the ratio of the pitch between the gaps ( $p$ ) to the spacing between the gaps and the conductor ( $s$ ) is an important parameter for fringing loss (Fig. 2.2); [9] recommends  $p < 4s$ .<sup>3</sup> For the proposed structure, we set the number of gaps equal to the number of turns ( $N_g = N$ ); Appendix A discusses how this selection, in tandem with the guidelines in Sections 2.2.4 and 2.2.5, generally meets the  $p < 4s$  criterion of [9].

<sup>2</sup>The simulations in Section 2.2 show this minimal impact on  $Q$  near the optimum. This claim is also supported by a prototype inductor with manufacturing tolerances achieving high  $Q$  in accordance with its simulated  $Q$  (see Section 3.2).

<sup>3</sup>While increasing the number of gaps at lower pitch reduces fringing loss, it does so with diminishing returns and also makes construction increasingly difficult. Moreover, there is indication that in some designs, use of additional magnetic pieces can increase effective core loss [26], though this was expressly not observed in the present work.

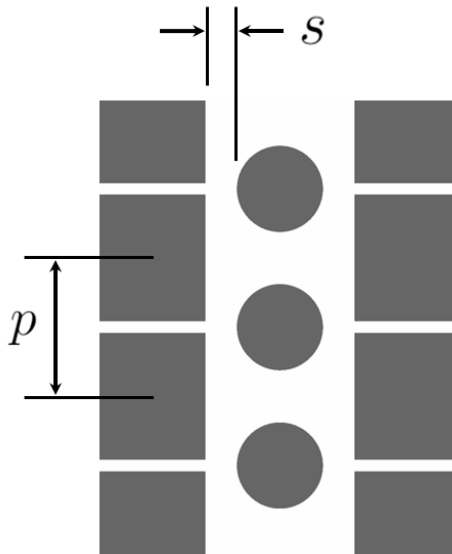


Figure 2.2: Two important parameters of quasi-distributed gaps are the pitch between the gaps ( $p$ ) and the spacing between the gaps and the conductor ( $s$ ). For an effective quasi-distributed gap with low fringing loss, the ratio of the pitch  $p$  to the spacing  $s$  should be  $p/s < 4$ , as recommended by [9].

### 2.2.2 Balance $H$ fields to achieve multi-sided conduction

Consider a single-layer solenoidal winding wrapped around the center post of a magnetic core (e.g. a drum core or pot core). For a single-layer winding, increases in copper loss at high frequencies over that at dc are primarily due to the skin effect, which reduces the effective area of current flow. At high frequencies, magnetic diffusion causes the current density to decay exponentially from the surface with a length constant of a skin depth  $\delta$ :

$$\delta = \sqrt{\frac{\rho}{\pi\mu f}} \quad (2.1)$$

where  $\rho$  is the resistivity of the conductor,  $\mu$  is the permeability of the conductor, and  $f$  is the frequency. This limited use of conductor cross-section significantly increases conduction losses compared to the uniform currents at dc [27].

In most inductor designs, only a single side of the wire carries current (within a skin depth of the surface), not the entire circumference, as is commonly shown in textbooks for a wire in isolation. This single-sided conduction occurs in typical inductor geometries because the  $H$  fields near the inner and outer sides of a given turn are imbalanced, causing uneven current distribution (Fig. 2.3a). Magnetic diffusion causes the currents in the conductor to flow in regions adjacent to high  $H$  fields near the conductor; this means that for a winding with unbalanced  $H$  fields on either side, the conduction currents are unevenly distributed between the two sides. To reduce copper loss, the geometry should instead be designed to balance the  $H$  fields near each turn. If the  $H$  fields on either side of a turn are balanced, double-sided conduction can be achieved, thus better distributing current for low loss (Fig. 2.3b).

The proposed structure implements double-sided conduction to achieve low copper loss. To balance the  $H$  fields in this structure, the center post and the return path need to have equal reluctances (Fig. 2.4). Doing so makes the MMF drop ( $\mathcal{F}$ ) across each region the same. Since both regions also have the same

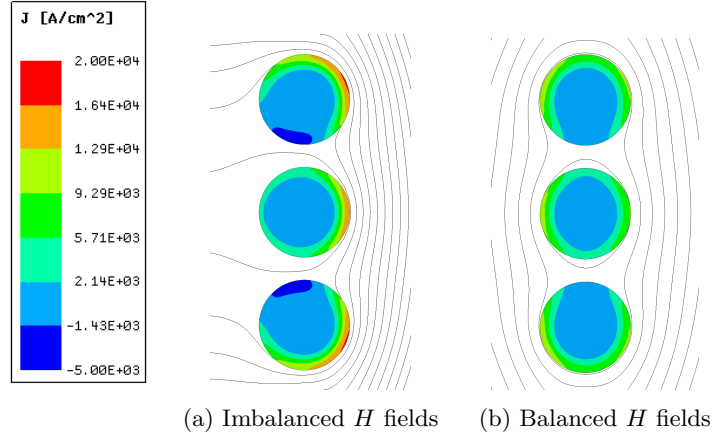


Figure 2.3: This figure shows field strength around a set of winding turns along with the current density within those turns.<sup>4</sup> When  $H$  fields are balanced, the effective conduction area in the winding is increased. A winding with a lower  $H$  field on one side than the other side has only single-sided conduction (2.3a), while a winding with comparable  $H$  fields on either side has double-sided conduction (2.3b). The field imbalance/balance can be seen in the plotted  $B$  field lines.

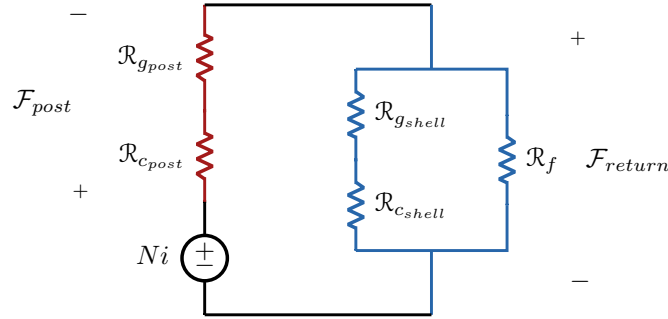


Figure 2.4: Magnetic circuit model used to balance the  $H$  fields in the proposed structure by making the reluctances of the center post (red) and return path (blue) equal. The discs of core material and the quasi-distributed gaps in the center post and the outer shell are treated as lumped reluctances. The end caps are composed of ungapped magnetic material and their reluctances are assumed to be negligible.

effective length ( $l$ ), having equal  $\mathcal{F}$  results in balanced  $H$  fields ( $\mathcal{F} = Hl$ ).

To accurately design for equal reluctances, we include the overall fringing field outside the structure in the return path. Mathematically, we need

$$\mathcal{R}_{c_{post}} + \mathcal{R}_{g_{post}} = (\mathcal{R}_{c_{shell}} + \mathcal{R}_{g_{shell}}) \parallel \mathcal{R}_f \quad (2.2)$$

where  $\mathcal{R}_{c_{post}}$  and  $\mathcal{R}_{c_{shell}}$  are, respectively, the lumped reluctances of the discs of core material in the center post and in the outer shell,  $\mathcal{R}_{g_{post}}$  and  $\mathcal{R}_{g_{shell}}$  are, respectively, the lumped reluctances of the quasi-distributed gaps in the center post and in the outer shell, and  $\mathcal{R}_f$  is the reluctance of the fringing path outside of the structure.

<sup>4</sup>For simulation and geometry details of this example simulation, see Appendix B.1.



Neglecting local gap fringing,  $\mathcal{R}_{c_{post}}$ ,  $\mathcal{R}_{c_{shell}}$ ,  $\mathcal{R}_{g_{post}}$ , and  $\mathcal{R}_{g_{shell}}$  can be calculated directly from the geometry (Fig. 2.1):

$$\mathcal{R}_{c_{post}} = \frac{l_c}{\mu_c \pi r_c^2} \quad (2.3) \quad \mathcal{R}_{c_{shell}} = \frac{l_c}{\mu_c \pi (r_t^2 - (r_c + w)^2)} \quad (2.4)$$

$$\mathcal{R}_{g_{post}} = \frac{l_g}{\mu_0 \pi r_c^2} \quad (2.5) \quad \mathcal{R}_{g_{shell}} = \frac{l_g}{\mu_0 \pi (r_t^2 - (r_c + w)^2)} \quad (2.6)$$

where  $l_c$  is the combined height of the core material discs,  $l_g$  is the overall length of the gap, and  $\mu_c$  is the permeability of the core material.

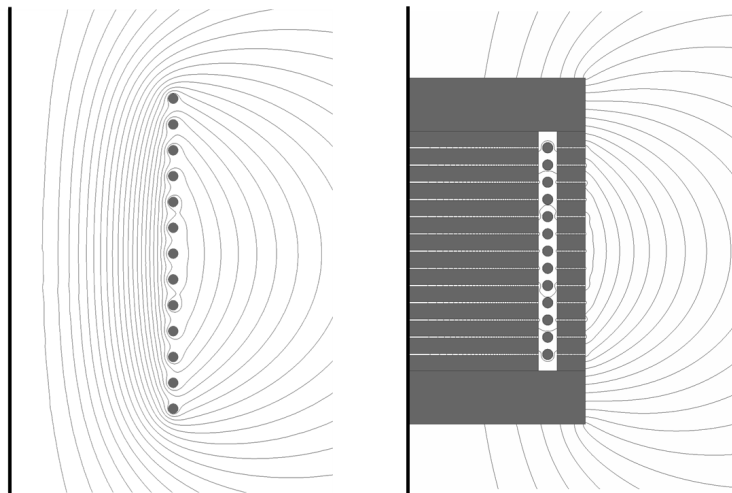


Figure 2.5: A coreless solenoid (left) and the proposed inductor (right) have similar fringing fields, as shown in the plotted  $B$  field lines, so the fringing field reluctances can be modeled as approximately equal. This approximation is then used in calculations for balancing the  $H$  fields in the proposed inductor.<sup>5</sup>

$\mathcal{R}_f$ , however, is more difficult to calculate from first principles; instead, we estimate it using a solenoid model. Since the proposed inductor and a solenoid of the same size have similar overall fringing fields (Fig. 2.5), their fringing field reluctances are about the same. So, to estimate  $\mathcal{R}_f$  of the proposed inductor, we can back out the fringing field reluctance from any appropriate solenoid inductance model. In general, for a solenoid,

$$L = \frac{N^2}{\mathcal{R}_{inside} + \mathcal{R}_f} \quad (2.7)$$

where  $\mathcal{R}_{inside}$  is the reluctance of the path through the center of the solenoid. By substituting a solenoid inductance model of our choosing into (2.7), we can then derive an expression for  $\mathcal{R}_f$ . For example, for structures where  $h_t > \frac{2}{3}r_t$ , the following air-core solenoid model [28] can be used:

$$L \approx \frac{\mu_0 N^2 \pi r_t^2}{h_t + 0.9r_t} \quad (2.8)$$

<sup>5</sup>For simulation and geometry details for this figure, see Appendix B.2.

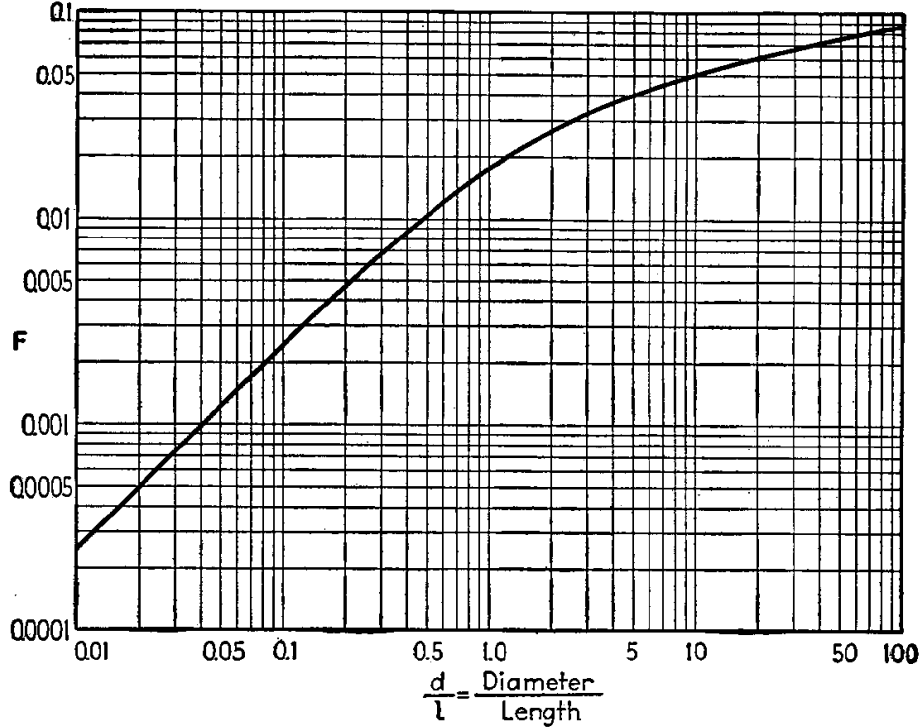


Figure 2.6: Plot of the experimental quantity  $F$  (in  $\mu\text{H}/\text{in}$ ) as a function of aspect ratio  $D/h_t$  (written as  $d/l$  in the plot), reproduced from Fig. 19 in [1]. Using this plot for the short solenoid model from [1], the fringing field reluctance  $\mathcal{R}_f$  can be estimated and used in calculations for achieving double-sided conduction.

Assuming that the reluctance in the barrel of the inductor  $\mathcal{R}_{inside} = h_t/(\mu_0\pi r_t^2)$ , we can then back out

$$\mathcal{R}_f \approx \frac{0.9}{\mu_0\pi r_t} \quad (2.9)$$

For more general cases, the short solenoid model [1] may be more appropriate:

$$\tilde{L} \approx 2FN^2\tilde{r}_t \quad (2.10)$$

where  $\tilde{L}$  is the inductance in  $\mu\text{H}$ ,  $\tilde{r}_t$  is the radius of the solenoid in inches, and  $F$  is an experimentally derived function of the aspect ratio  $D/h_t$  in  $\mu\text{H}/\text{in}$ , which is both tabulated and plotted in [1]. Fig. 2.6 reproduces the plot from [1] for reference. With this model,

$$\mathcal{R}_f \approx \frac{2.54 \times 10^4}{2r_tF} - \frac{h_t}{\mu_0\pi r_t^2} \quad (2.11)$$

Using  $\mathcal{R}_f$ , we can then design the center post and the return path to have equal reluctances, and thus balance the  $H$  fields to achieve double-sided conduction.

To validate this approach for estimating  $\mathcal{R}_f$ , inductors of the same volume ( $14\text{ cm}^3$ ) but different aspect ratios were designed for the same inductance ( $16.6\ \mu\text{H}$ ) using Eq. (2.9). The inductors were then simulated, and the designed and simulated inductances had less than 10% error across a wide range of aspect ratios (Table 2.1).<sup>6</sup>

<sup>6</sup>For full simulation and geometry details of the inductors simulated for Table 2.1, see Appendix B.

Table 2.1: Error of inductance model (Section 2.2.2) for 16.6  $\mu\text{H}$  designs

aspect ratio ( $h_t/(2r_t)$ )	simulated $L$ ( $\mu\text{H}$ )	error (%)
1/3	17.4	4.6
0.5	18.0	8.5
1.0	17.0	2.4
1.5	16.2	2.7
2.0	16.7	0.3

### 2.2.3 Distribute $B$ fields to reduce overall core loss

While  $H$  field balancing helps prevent circulating current losses in the winding, evenly distributed  $B$  fields in the core can reduce core loss. In the case of unevenly distributed  $B$  fields, regions with higher  $B$  fields experience much greater core loss, since core loss scales as  $B^\beta$  (for high-frequency ferrites,  $\beta \approx 2-3$ ). The high core losses in these regions then result in greater total core loss than if the  $B$  field was more uniformly distributed.

Since  $B = \mu H$ , regions with the same permeability and  $H$  fields will have the same  $B$  fields. In the proposed inductor, the center post and the outer shell have the same effective permeability because they have the same overall gap and core lengths. Therefore, designing for balanced  $H$  fields in the proposed structure will also achieve evenly distributed  $B$  fields in these core regions. For cases in which the center post and the outer shell do not have the same effective permeability, the structure cannot achieve both balanced  $H$  fields and evenly distributed  $B$  fields. Instead, to minimize overall loss, the designer would need to find the optimal balance with partial double-sided conduction and a slight imbalance in the  $B$  field distribution.

For the end caps, the  $B$  field distribution, and thus core loss, is affected by their thickness. Thicker end caps allow the flux to distribute more in these regions for lower core loss, but with diminishing returns for added volume. The designer can use simulation to determine an end cap thickness that reduces loss without excessive volume. A good heuristic starting point is to pick an end cap thickness that is  $\sim h_t/6.5$ .

### 2.2.4 Select a wire size that optimizes effective conduction area

Since the structure is designed to achieve double-sided conduction in the winding, larger diameter wire reduces copper loss by providing more circumferential conduction area. As the wire diameter increases, however, proximity effect losses between the turns play a larger role.

One metric for selecting a wire diameter ( $D_w$ ) is the vertical window fill ( $F_v$ ), defined as the fraction of the window height ( $l_t$ ) that is occupied by conductive material, i.e.

$$F_v = \frac{ND_w}{h_t - 2h} \quad (2.12)$$

using the geometry in Fig. 2.1 and neglecting wire insulation thickness. Finite element analysis (FEA) simulations<sup>7</sup> show that a wire diameter yielding a vertical window fill between 50–80% optimizes the total effective conduction area for these two competing effects (Fig. 2.7). For a given window height, the copper loss is largely insensitive to deviations in the wire diameter near the optimum.

<sup>7</sup>All FEA simulations were run in ANSYS Maxwell 2D Design, Versions 18.2 and 19.2, except for those in Section 3.3 which were run in Finite Element Method Magnetism (FEMM).

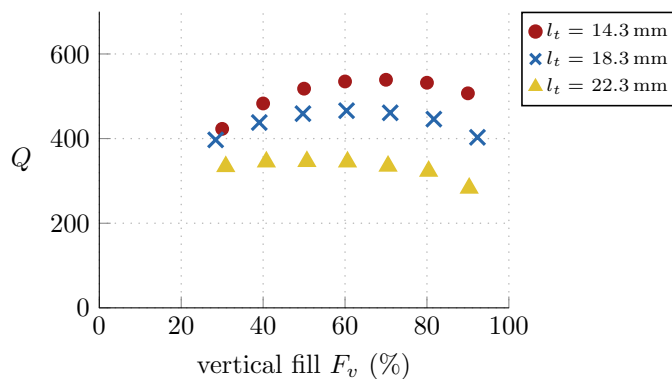


Figure 2.7: For a given window height  $l_t$ , a wire diameter that yields a 50–80% vertical window fill optimizes the total effective conduction area to reduce copper loss. This optimal range holds across different window heights. To find this optimum, inductors with the same inductance (16.1  $\mu\text{H}$ ) and core geometry ( $r_t = 13.2$  mm,  $h_t = 26.3$  mm) but different conductor diameters were simulated.<sup>8</sup> For negligible gap fringing loss, the inductors had a large window width that was 3 times the maximum wire diameter at  $F_v = 100\%$ .

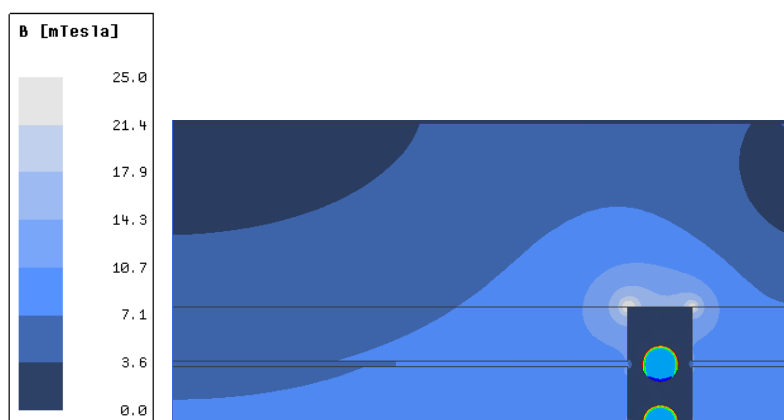


Figure 2.8: Flux crowding at the end of the window leads to higher  $B$  fields (grey) and thus greater core loss.<sup>9</sup>

### 2.2.5 Select a window size that balances gap fringing field loss and core loss in end caps to reduce overall loss

To minimize gap fringing field loss, the structure would ideally have a large window to increase the horizontal distance between the gaps and the winding. However, since flux crowding around the ends of the window leads to higher  $B$  fields in and near the end caps (Fig. 2.8), a larger window would increase core loss by increasing the volume of these high- $B$ -field regions.

One metric for selecting a window width ( $w$ ) is the horizontal window fill ( $F_h$ ), defined as the fraction of the window width that is occupied by conductive material, i.e.

$$F_h = \frac{D_w}{w} \quad (2.13)$$

<sup>8</sup>For simulation and geometry details of these simulated points, see Appendix B.4.

<sup>9</sup>This figure is a close-up view of Fig. 3.1a.

using the geometry in Fig. 2.1 and neglecting wire insulation thickness. FEA simulations show that to balance the fringing loss and the end cap core loss, the horizontal window fill of the winding should be between 40–60% (Fig. 2.9). So, for a given wire diameter  $D_w$ , the optimal window size is approximately  $2D_w$ , but the overall loss is largely insensitive to changes in the window size near the optimum.

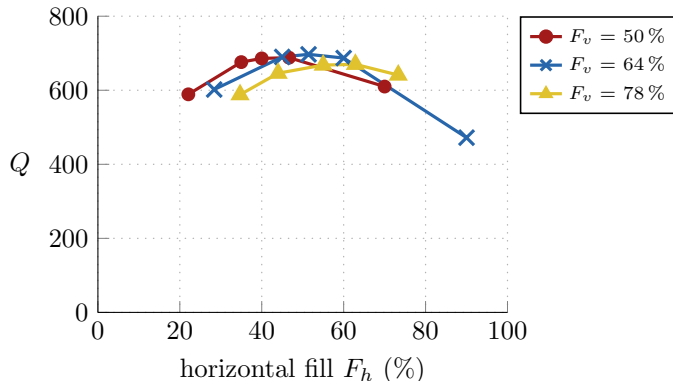


Figure 2.9: For a given wire diameter, a window size with a 40–60% horizontal fill for the winding balances the gap fringing loss and end cap core loss. This optimal range holds across the optimal vertical fill ( $F_v$ ) range. To find this balance, inductors with the same inductance (16.5  $\mu\text{H}$ ) and volume ( $r_t = 13.2$  mm,  $h_t = 26.3$  mm) but different window widths were simulated.<sup>10</sup>

### 2.2.6 Use a square aspect ratio to minimize overall loss

A “square” aspect ratio (diameter  $\approx$  height) is the preferred overall geometry for this structure. FEA simulations of otherwise optimized inductors show that structures that are much wider than they are tall, or vice-versa, achieve lower  $Q$  (Fig. 2.10).

Conceptually, we can explain the disadvantages of unbalanced geometries by considering the end caps separately from the rest of the structure (everything within  $l_t$ ). The section within  $l_t$  may be thought of as the “active” section where flux links the winding and substantial reluctance is provided, while the end caps may be thought of as overhead required to complete the magnetic path. These two sections have opposite loss dependencies on diameter: increasing diameter increases loss in the end caps by adding volume (for a fixed end cap height) but decreases loss in the active section.<sup>11</sup> This competing tendency explains why intermediate aspect ratios provide the best performance.

### 2.2.7 Approximately balance copper and core loss to reduce overall loss

In general, for a given core material, the number of turns and overall gap length in an inductor can be used to tune the copper and core losses. Decreasing the number of turns decreases the copper loss, but to maintain the same inductance, the overall gap length must also decrease, which increases the  $B$  field and thus core loss. Conversely, increasing the overall gap length decreases the core loss at the expense of increasing copper loss.

<sup>10</sup>For simulation and geometry details of these simulated points, see Appendix B.5.

<sup>11</sup>For a first-order derivation showing that loss in the active section decreases as diameter increases, see Appendix C.

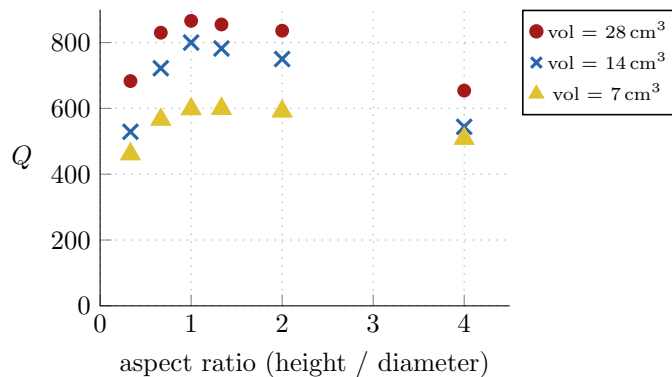


Figure 2.10: Structures with a “square” aspect ratio achieve the optimum  $Q$ . To find this optimum, inductors with different aspect ratios but the same inductance ( $16.5 \mu\text{H}$ ) and volume were simulated,<sup>12</sup> and each design was optimized using the guidelines discussed in Sections 2.2.1 to 2.2.7. As shown in the graph, the “square” aspect ratio is optimal across different volumes.

For inductors in which ac losses are dominant considerations over dc losses or saturation, the overall loss is usually minimized at a point where core loss is close to, but slightly less than copper loss [29]. To reduce the overall loss in the proposed structure, the designer can balance the copper and core losses accordingly by modeling the losses with exact core loss parameters and/or by hand-tuning the design in simulation, as is often done in conventional inductor designs.

For Fair-Rite 67 material ( $\mu_r = 40$ ) at 3 MHz, a good heuristic starting point is to pick the number of turns such that the overall gap length is  $\sim 10\%$  of the overall core length. For the same material at different frequencies, different heuristics would be needed due to the change in core loss behavior, particularly  $\beta$ , across frequency as well as the change in skin depth, which affects winding loss. Different heuristics would also be needed for other materials that have different core loss characteristics.

## 2.3 Automating initial designs of the proposed structure

Using the design guidelines discussed in Section 2.2, we can mathematically define the proposed inductor geometry. The design process can then be largely automated to generate high- $Q$  inductor designs for a desired volume and inductance at a given frequency and current (Fig. 2.11). The end cap height and the number of turns, however, must still be manually tuned. An example Python script for automating the design process can be found in Appendix D.

<sup>12</sup>For simulation and geometry details of these simulated points, see Appendix B.6.

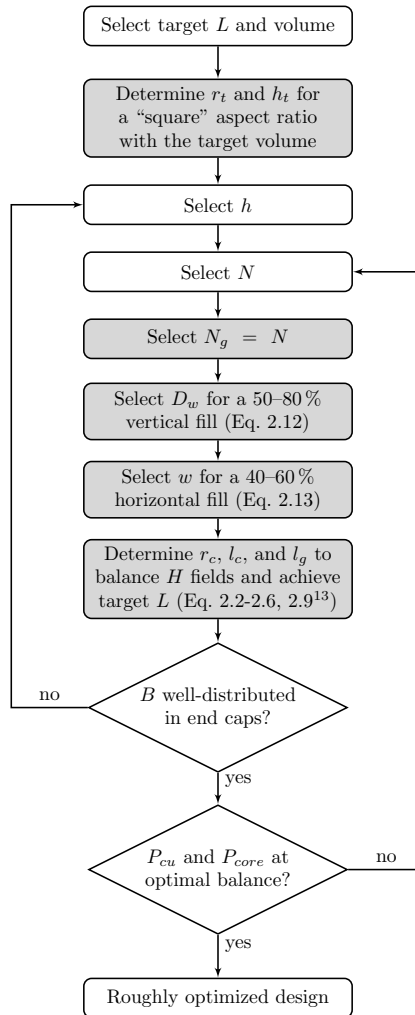


Figure 2.11: Flowchart of the design process for the proposed inductor structure using the guidelines from Section 2.2. The parameters used in the flowchart are labelled on the cross-sectional view in Fig. 2.1. Grey fill denotes steps that can be automated.

<sup>13</sup>Eq. 2.9 may be replaced with Eq. 2.11 or any other appropriate fringing field reluctance model.





## Chapter 3

### An Example 16.6 $\mu\text{H}$ Design

Using the guidelines in Section 2.2, we designed an example 16.6  $\mu\text{H}$  inductor that achieved a  $Q$  of 700 at 3 MHz and 2 A (peak) of ac current in FEA simulation (Table 3.1). To design the example inductor, a script was used. The target inductance and volume as well as a selected  $h$  and  $N$  were entered into the script, which generated dimensions for the geometry that were then simulated. Afterwards, the height of the end caps was manually tuned for well-distributed  $B$  fields, such that additional height would only slightly further distribute the fields and thus marginally reduce core loss in the end caps. The script was re-run with the optimized  $h$ . Next, designs with varying number of turns were generated using the script to find the optimum core and copper loss balance for minimum total loss. At this point, the example design was roughly optimized. We then chose to continue with additional minor adjustments in FEA for further optimization (Table 3.2).

Table 3.1: Specifications for the simulated example inductor

Inductance	16.6 $\mu\text{H}$
Frequency	3 MHz
Current	2 A (peak, ac)
Core Material	Fair-Rite 67, $\mu_r = 40$ Steinmetz parameters: $k_c = 0.034$ , $\alpha = 1.18$ , $\beta = 2.24$ ( $P_v$ in $\text{mW}/\text{cm}^3$ , $f$ in MHz, $\hat{B}$ in mT)

Table 3.2: Geometry of the simulated example inductor (see Fig. 2.1)

Total Diameter ( $2r_t$ )	26.9 mm
Centerpost Radius ( $r_c$ )	9.9 mm
Window Width ( $w$ )	1.4 mm
Total Height ( $h_t$ )	26.0 mm
End Cap Height ( $h$ )	4.0 mm
Total Core Length ( $l_c$ )	16.5 mm
Total Gap Length ( $l_g$ )	1.5 mm
Number of Turns ( $N$ )	13
Number of Gaps ( $N_g$ )	13
Wire Diameter ( $D_w$ )	0.812 mm (20 AWG)

### 3.1 Simulation Results

Simulation results verified that by following the design guidelines, the example design achieved all of the desired low-loss features, and thus a roughly optimized  $Q$ . The  $B$  fields in the center post and the shell were roughly equal for low core loss (Fig. 3.1a), and most turns had balanced  $H$  fields and associated double-sided conduction for low copper loss (Fig. 3.1b). It was verified that additional thickness to the end caps would have minimal effect on loss, and that larger or smaller window sizes would increase total loss. The core and copper loss were also verified to be well balanced.

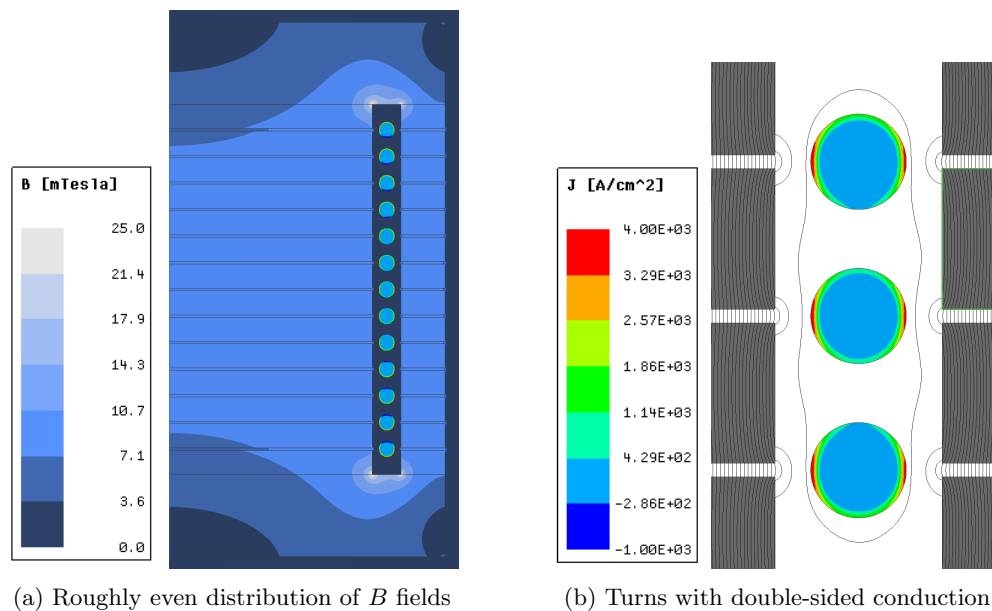


Figure 3.1:  $B$  field (blue),  $B$  field lines (black), and current distribution (rainbow) simulations of the example  $16.6\ \mu\text{H}$  inductor verifying that it achieves the desired low-loss features by following the design guidelines in Section 2.2. These 2D axisymmetric simulations are designed to capture the “worst-case” distributions for a helical winding, with each turn next to a gap. Other cross sections of the inductor would have turns in between the gaps and thus lower loss.

## 3.2 Experimental Results

We constructed a prototype (Fig. 3.2) of the example inductor presented in Section 3.1.<sup>1</sup> The prototype inductor achieved a large-signal quality factor measurement<sup>2</sup> of  $Q = 720$  at 3 MHz and 2 A (peak) of ac current (Table 3.3), which agrees with simulations. In addition, the prototype continued to have high  $Q$  outside of its optimized designed operating point. In this section, we demonstrate the performance of the inductor across drive level and at higher frequencies. We also show the prototype improving the efficiency and thermal performance of a high-current-swing power converter.

Table 3.3: The simulated example inductor and the prototype with 20 AWG wire

	Simulated	Prototype
Inductance	$16.6\ \mu\text{H}$	$13.4\ \mu\text{H}$ <sup>3</sup>
$Q$ at 3 MHz, 2 A (pk, ac)	700	720

<sup>1</sup>For fabrication details of the prototype inductor, see Appendix E.

<sup>2</sup>For details on the large-signal  $Q$  measurement approach, see Appendix F.

<sup>3</sup>The discrepancy between the simulated and prototype inductances can be partly attributed to permeability variations (a 25% variation yields a 7% error) and to the added vertical windows in the outer shell, which were not included in 2D simulation (yields a 2% error). The plastic shimstock used for the gaps also had thickness tolerances ranging from 6.7–13.3%, which could contribute to the inductance discrepancy.



Figure 3.2: Prototype inductor of the example design (Section 3.1) having a measured  $Q$  of 720. Vertical windows in the outer shell were added to impede the circumferential component of flux and to allow the winding terminations to leave the structure.

### 3.2.1 Experimental $Q$ measurements of the prototype verified simulations

The  $Q$  of the prototype inductor was measured across drive levels (0.5–3.5 A), and the experimental measurements closely matched the simulated quality factors (Fig. 3.3). This agreement experimentally verified the simulations, and the experimental  $Q$  measurements also verified that the guidelines in Section 2.2 achieve a high  $Q$  inductor.<sup>4</sup>

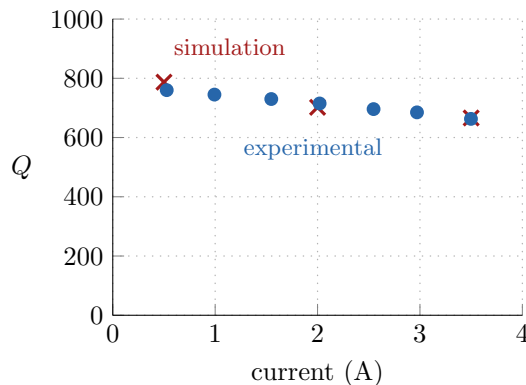


Figure 3.3: The experimental  $Q$  measurements of the prototype inductor (Fig. 3.2) closely matched the simulated quality factors, thereby verifying the simulations and demonstrating that the guidelines in Section 2.2 can achieve a high  $Q$  inductor.

### 3.2.2 Prototype inductor achieves high $Q$ at higher frequencies

The features that allow the prototype inductor to achieve high  $Q$  at 3 MHz, namely double-sided conduction and quasi-distributed gaps, continue to be beneficial at higher frequencies. In simulations at 4.5 MHz and 5.5 MHz<sup>5</sup>, the example inductor achieved high quality factors ( $Q \approx 700$ ) at 2 A (peak) of ac current (Fig. 3.4). The prototype inductor also had measured quality factors of  $Q \approx 700$  at these two frequencies, demonstrating the structure’s potential to achieve high  $Q$  at higher frequencies.

<sup>4</sup>In some MnZn ferrite quasi-distributed designs, increased surface losses from multiple gaps have been observed [26, 30]. For the prototype inductor, however, the agreement between the experimental and simulated quality factors indicates that any surface loss effects are minimal.

<sup>5</sup>For 4.5 MHz and 5.5 MHz, the Steinmetz parameters were  $k_c = 0.00163$ ,  $\alpha = 1.37$ , and  $\beta = 2.21$  (for  $P_v$  in  $\text{mW}/\text{cm}^3$ ,  $f$  in MHz,  $\hat{B}$  in mT). The parameters were derived using core loss data for Fair-Rite 67 from [11].

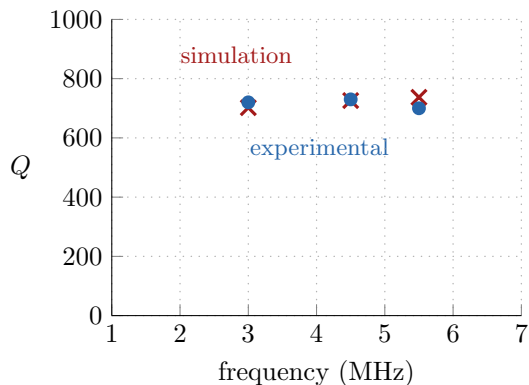


Figure 3.4: The prototype inductor (Fig. 3.2) continued to have high quality factors at frequencies higher than its designed frequency of 3 MHz. Simulations and measurements were taken at 2 A (peak) of ac current.

### 3.2.3 Prototype inductor improved efficiency of a high-current-swing power converter

In addition to achieving a high  $Q$  under controlled conditions, the example inductor was used in a power factor correction converter operating at dynamically varying frequencies of 1–3 MHz and with large ac current components in the inductor [31]. The inductor improved converter performance significantly (Fig. 3.5) over a more conventional open-magnetic-circuit inductor (a half-toroid core approximating a rod core with litz wire) (Table 3.4), despite having similar effective volume. This improvement can also be seen in thermal measurements: at a 93 W operating point, the conventional inductor saw a  $\sim 30^\circ\text{C}$  temperature rise, while at a much higher power (296 W), the proposed inductor only saw a  $\sim 3^\circ\text{C}$  rise (Fig. 3.6).

Table 3.4: Specifications for the conventional inductor

Inductance	15 $\mu\text{H}$
Core Material	Fair-Rite 67, $\mu_r = 40$
Core Geometry	half-toroid (approximating a rod): $ID = 23\text{ mm}$ , $OD = 35.55\text{ mm}$ , $h = 12.7\text{ mm}$
Wire	5/9/10/48 litz (26 turns)

## 3.3 Litz Wire in the Proposed Structure

While the example inductor in Section 3.1 can achieve low winding loss through double-sided conduction, a large fraction of the solid-core winding cross-sectional area still remains unused. In some cases, litz wire can have greater effective conduction area for improved performance in the proposed structure. For example, a litz wire version of the prototype inductor (Fig. 3.2) achieved a higher  $Q$  of 980 at the same frequency and drive level (3 MHz, 2 A (peak) of ac current). In this section, we describe design guidelines for optimizing litz wire and discuss the improved simulation and experimental results of the example inductor with litz wire.<sup>6</sup>

<sup>6</sup>This work was carried out in close collaboration with researchers at Dartmouth, who co-authored the associated publication [23], and is reported here for completeness.

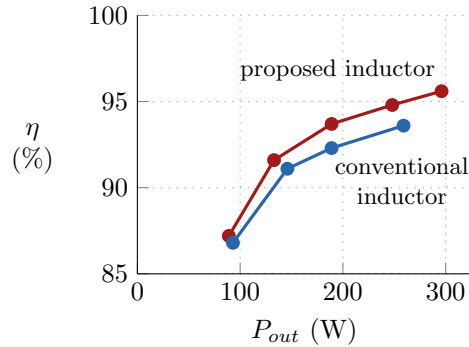


Figure 3.5: The proposed inductor improved the efficiency of a power converter operating at 1–3 MHz at different output powers, compared to a conventional inductor.

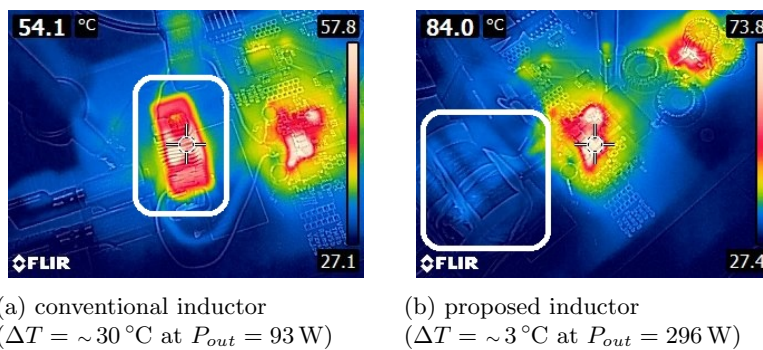


Figure 3.6: Thermal images showing the proposed inductor (3.6b, white box) having a much smaller temperature rise for a higher converter output power than a more conventional open-magnetic-circuit inductor (3.6a, white box).

### 3.3.1 Design guidelines for optimizing litz wire

As a starting point, the simple design procedure for economical litz wire presented in [32] can be used to optimize litz wire. For a given winding window, the procedure optimizes the number of strands and strand diameter for loss and cost. To estimate power loss, the ac resistance factor ( $F_R$ ) is used and can be calculated by

$$F_R = \frac{R_{ac}}{R_{dc}} = 1 + \frac{(\pi n N_s)^2 d_s^6}{192 \cdot \delta^4 b^2} \quad (3.1)$$

where  $\delta$  is the skin depth,  $b$  is the breadth of the winding window,  $N_s$  is the number of turns,  $n$  is the number of strands, and  $d_s$  is the strand diameter. When the strand diameter is close to or greater than the skin depth, however, (3.1) may not be accurate. Instead, the semi-empirical approach from [33] can be used to better estimate power loss.

The simple litz design procedure is useful, but it is agnostic to the construction of the litz wire, which can affect performance when  $d_s$  is not much less than  $\delta$ , as may frequently be the case in high-frequency designs. Litz wire is constructed from strands of individually insulated wire that are twisted together into bundles; multiple bundles may be twisted together to form a larger effective wire, and such second-level bundles may also be twisted together to increase the effective wire size further. Thus, there are many ways to construct litz wire for a given number of strands and strand diameter. Since each level of bundling may experience skin and proximity effects similar to those experienced by solid core wire [34], the choice of construction can

be important. To mitigate bundle-level skin effect, [32] recommends that the number of strands in the first twisting operation should be less than

$$n_{1,max} = 4 \frac{\delta^2}{d_s^2} \quad (3.2)$$

Subsequent twisting operations should combine no more than five bundles. If for some reason these guidelines cannot be followed (e.g., using a standard litz wire design to reduce cost), bundle-level skin effect losses are no longer negligible and should be included when estimating power loss [33, 35].

In addition, when the strand diameter is close to or larger than the skin depth, the way the strands are twisted together can be important and should be included when estimating power loss. Bundles may be “bunched” together (indicated by the “/” symbol), meaning that the bundles are twisted in the same direction as the prior level bundles/strands. Alternatively, bundles may be “cabled” together (indicated by the “×” symbol), meaning that the bundles are twisted in the opposite direction. For example, the  $5 \times 9 \times 10/48$  configuration in Fig. 3.7a is 10 strands of 48 AWG wire bunched together, then 9 of those bundles cabled together, and finally 5 of those bundles cabled together. The  $5/9/10/48$  configuration in Fig. 3.7b has the same number of strands and bundles as  $5 \times 9 \times 10/48$ , but is bunched in each twisting operation rather than cabled. In this example, bunching achieves higher packing factor than cabling.

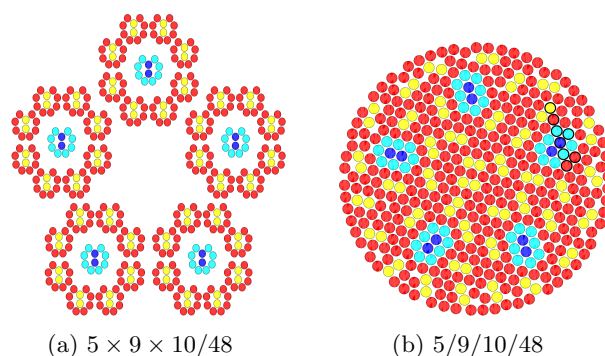


Figure 3.7: Idealized cross-sections of litz wires with 450 strands using (a) cabling and (b) bunching twisting operations. The different colors of strands correspond to different circuit “shells” used to simulate bundle-level skin effect [33].

### 3.3.2 Simulations showed litz wire improving $Q$ of prototype inductor at 3 MHz

Using the guidelines in Section 3.3.1, we investigated the effect of different litz wire designs on the performance of the example inductor (Section 3.1) at 3 MHz. For these designs, we chose strands of 48 AWG since they are a good trade-off between cost and power loss at this frequency.<sup>7</sup>

First, we used the simple litz wire design procedure [32] to estimate the optimal number of strands. Since the strand diameter is close to the skin depth at 3 MHz, we then used the semi-empirical approach from [33] to more accurately find an approximately optimal number of strands (275) and construction ( $5 \times 5 \times 11/48$ ). We also used this approach to simulate a configuration that was readily available for experimental verification (450 strands, constructed as  $5/9/10/48$ ) (Fig. 3.7b). Since the  $5/9/10/48$  configuration is more susceptible to bundle-level skin effect, it was simulated with bundle-level skin effect (worst case) and without it (best case). Because of random perturbations in the positions of the strands in real litz wire, some bundle-level

<sup>7</sup>Power loss could be further reduced with finer strands; however, the costs of magnet wire manufacturing and litz construction increase rapidly for strands with wire gauge greater than 44 AWG.

skin effect may be mitigated, and it is expected that experimental results will fall between the worst and best cases.

Simulation results show that litz wire can provide significant improvement over solid wire for the example inductor used throughout this paper (Fig. 3.8). The approximately optimal configuration ( $5 \times 5 \times 11/48$ ) performs slightly better<sup>8</sup> in simulation than the simple litz model prediction by 7.9%, due to the self shielding effect that occurs when the strand diameter is close to the skin depth [33]. The readily available 5/9/10/48 configuration under-performs the simple litz model by 6.6% when bundle-level skin effect is included.

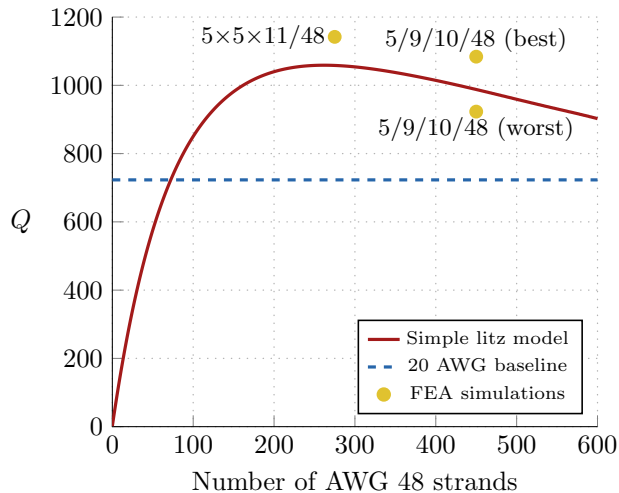


Figure 3.8: Simulated inductor  $Q$  versus number of AWG 48 litz wire strands using a simple design method (red line) and FEA simulations of specific litz configurations (yellow points) at 3 MHz and 2 A (peak) of ac current. At this operating point, the example inductor can achieve higher  $Q$  with litz wire than with 20 AWG solid wire (blue dashed line).

### 3.3.3 Experimental $Q$ measurements of litz wire prototype verified simulations

Using the same core geometry as the example inductor presented in Section 3.1, we constructed a prototype inductor with the readily available 5/9/10/48 litz wire. At 3 MHz and 2 A (peak) of ac current, the litz wire prototype achieved an experimental quality factor of  $Q = 980$ , agreeing with simulations (Table 3.5). For this operating point, litz wire provided a 36% improvement in  $Q$  over solid-core wire. This improvement demonstrates the potential of litz wire to improve performance of the proposed structure for certain operating points.

Table 3.5: The simulated example inductor and the experimental prototype with 5/9/10/48 litz wire

	Simulated (average case)	Prototype
Inductance	16.6 $\mu\text{H}$	12.6 $\mu\text{H}$
$Q$ at 3 MHz, 2 A (peak, ac)	1000	980

<sup>8</sup>While the number of strands in the first twisting operation is higher than the recommendation from (3.2) ( $n_{1,max} = 5$  at 3 MHz), it does not result in significant bundle-level skin effect in this case (a difference of 0.96% in  $Q$ ).

### 3.3.4 Litz wire prototype can achieve high $Q$ at high frequencies

At higher frequencies (up to 5.5 MHz), the litz wire prototype continued to achieve high  $Q$  at 2 A (peak) of ac current. However, since the litz wire in the prototype inductor was designed for 3 MHz, the performance using this particular construction (5/9/10/48) over 20 AWG wire declined at higher frequencies (Fig. 3.9). Other litz wire configurations optimized for higher frequencies, e.g. with fewer number of strands, could have lower high-frequency copper loss, and litz wire may still be beneficial at higher frequencies [33].

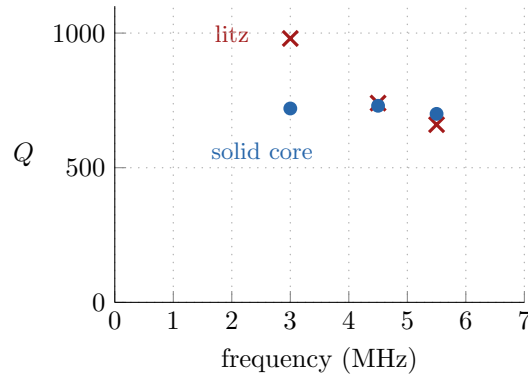


Figure 3.9: Experimental results: Using 5/9/10/48 litz wire instead of 20 AWG solid-core wire in the prototype inductor improved its  $Q$  at 3 MHz. This litz wire configuration, though, had worse performance above its optimized frequency of 3 MHz.



## Chapter 4

# Design and Application Flexibility of the Proposed Structure

In Chapter 3, we investigated the performance of a single design using the proposed inductor structure and design guidelines, and demonstrated that it achieves high  $Q$ . In this chapter, we expand our focus to evaluate the performance and limitations of the structure across a range of inductor requirements. We then investigate approaches that can use a relatively small set of components to cover a wide range of requirements. With these approaches, the proposed structure and design techniques have greater potential for commercial adoption.

### 4.1 Design Flexibility of a Single Core Set

The core geometry of the proposed structure has three types of magnetic parts: (1) the center disc, (2) the outer shell, and (3) the end cap (Fig. 4.1). (This is in addition to non-magnetic spacers which form the gaps.) For a particular design with specified dimensions for each part, the collection of these parts is called a *core set*. A core set also has a particular *footprint*, defined by the diameter of the end cap. For example, the 16.6  $\mu\text{H}$  design from Chapter 3 is constructed from a single core set with a 26.9 mm-diameter footprint, which we will call the *MP27 core set* because its overall footprint is approximately 27 mm in diameter.

In this section, we evaluate the performance and limitations of the MP27 core set by determining the inductance and power handling range for which the core set can continue to achieve low loss, considering the ability to adjust the number of turns of the winding, the number of discs and spacers, and the spacer length. For this evaluation, a temperature rise constraint of  $\Delta T \leq 40^\circ\text{C}$  was imposed using a constant heat flux model.<sup>1</sup>

#### 4.1.1 Inductance Range

First, we investigated the inductance range of a single core set at a fixed energy storage and frequency (or fixed power handling<sup>2</sup>). In this case, the constant temperature rise constraint is equivalent to a constant  $Q$  constraint.

---

<sup>1</sup>For details on the constant heat flux model used, see Appendix G. Constant heat flux as a thermal constraint was also adopted in [36].

<sup>2</sup>This thesis uses VA as the equivalent metric for power handling of sinusoidal waveforms, where  $VA = V_{rms} \cdot I_{rms} = (2\pi f\lambda)I_{rms} = 2\pi fLI_{rms}^2 = \pi fLI^2$  and  $I$  is the amplitude of the sinusoidal current.

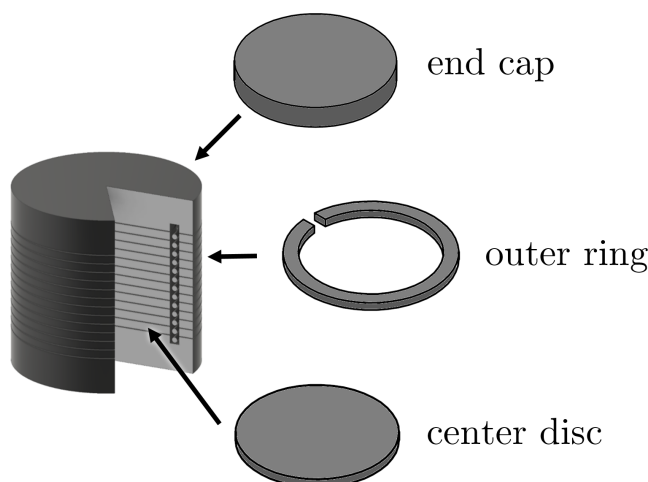


Figure 4.1: A single core set is composed of three types of magnetic parts: the center disc, the outer shell, and the end cap. The outer shell may be realized as an outer ring with a notch cut out to allow for the winding terminations to leave the structure (as shown in this figure).

For a given core geometry, the inductance can be changed by changing the number of turns and/or the overall length of the gap. The number of turns can be thought of as a coarse tuning knob for changing the inductance, while the gap length handles fine tuning. For a fixed number of core discs (and outer shell pieces), changing only the gap length leads to a very limited change in the inductance. A large change in gap length greatly changes the core and copper loss distribution in the inductor, causing the  $Q$  to deviate from optimum significantly. Since the gap length is a continuous parameter, though, it is useful for fine tuning the inductance.

Changing only the number of turns (and adjusting the conductor diameter accordingly), however, does not significantly redistribute the core and copper losses for a wide range of inductances. For a constant energy storage and fixed gap length, the  $B$  fields, and thus the core loss, do not vary much with the number of turns. In a single-layer winding with double-sided conduction, changing the number of turns also does not greatly change copper loss. While the conductor resistance scales as  $N^2$  with inductance, the current scales as  $1/N$  for constant peak energy storage, leading to the two factors roughly cancelling in power loss,  $i^2R$ . This cancellation, however, has an upper limit and begins to fall off when the diameter of the conductor approaches the skin depth, as the resistance scales faster than  $N^2$ , leading to lower  $Q$ .

The lower limit of the inductance range depends on the window width of the core geometry. As the number of turns decreases, the diameter of the conductor is increased to compensate for the increase in current to maintain a constant energy storage. At a certain point though, the desired diameter is impractical for the window, as too large of a diameter brings the conductor extremely close to the gaps, leading to greater fringing loss. Even without fringing loss considerations, there is still the physical constraint of the diameter needing to be smaller than the window. Because of this limitation, the window is not well-utilized for small numbers of turns, leading to increased copper loss and lower  $Q$ .

To instantiate the above analysis, we evaluated the achievable inductance range of the MP27 core set configuration used in the example  $16.6\mu\text{H}$  design from Chapter 3 at 3 MHz. This configuration has an

aspect ratio of  $h/D = 1$ . Fig. 4.2 plots the configuration's maximum power handling curve across a range of inductances, where the structure is at the maximum allowable temperature rise of  $\Delta T = 40^\circ\text{C}$ . The range of achievable requirements of the configuration is then the area underneath this curve. At the maximum power handling of  $\sim 1000\text{ VA}$ , the configuration can cover a factor-of-50 range of inductances. For lower power handling requirements, the configuration can cover an even wider range of inductances. Inductances less than  $\sim 10\ \mu\text{H}$  have lower power handling capability because the vertical window fill factor  $F_v$  drops below 0.5, which is outside the optimal range. On the other end, inductances greater than  $\sim 1.5\text{ mH}$  have lower power handling because the winding diameter drops below  $90\ \mu\text{m}$ , which is on the order of a skin depth at  $3\text{ MHz}$  ( $37.6\ \mu\text{m}$ ). Since the limitations of the inductance range are not specific to this particular configuration, we can expect a similarly wide inductance range coverage for other configurations, which is confirmed in later sections of this chapter.

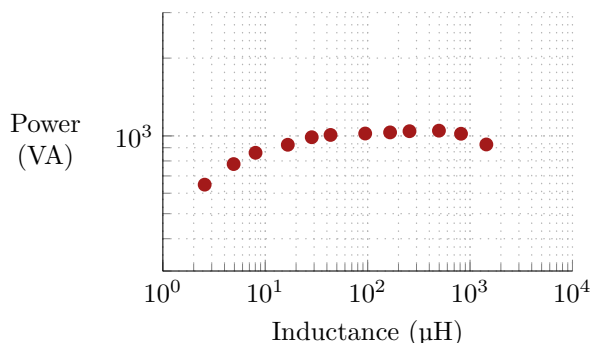


Figure 4.2: Maximum power handling curve at  $\Delta T = 40^\circ\text{C}$  of the MP27 core set at  $h/D = 1$ . This core set configuration can cover a factor-of-10 range of inductances at the maximum power handling of  $\sim 1000\text{ VA}$  and can cover an even wider range at lower power handling requirements.

### 4.1.2 Power Handling Range

For a given core set, the volume of the inductor structure can be changed by changing the number of stacked core pieces in the center post and outer shell. The aspect ratio ( $h/D$ ) of the structure also scales with volume. For example, scaling the volume of the structure by a factor of 2 also scales the aspect ratio by a factor of 2. Through changing the volume, the power handling capability of the structure changes accordingly.

To get a better idea of the achievable range of inductor requirements for the MP27 core set, structures with different aspect ratios (and volumes) were evaluated across a range of inductances within the temperature rise constraint  $\Delta T \leq 40^\circ\text{C}$  (Fig. 4.3). Each curve represents the maximum power handling of the corresponding aspect ratio of the structure. The lower bound of the aspect ratio ( $h/D = 0.4$ ) is set by the height of two stacked core pieces with a single gap, while the upper bound ( $h/D = 3.0$ ) is set by practical considerations of desired inductor shapes. Each aspect ratio curve covers a wide range of inductances, as predicted in Section 4.1.1. It's difficult, though, to evaluate the most effective power handling range of the MP27 core set by looking at this plot alone. For better evaluation, this core set must be compared against core sets with different footprints, as shown in the next section.

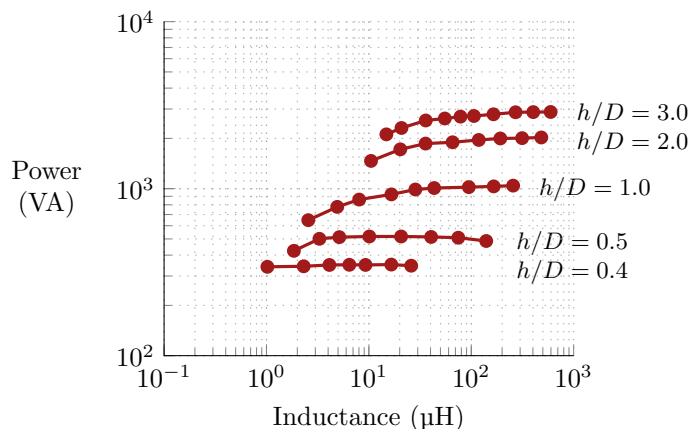


Figure 4.3: Maximum power handling curves at  $\Delta T = 40^\circ\text{C}$  of the MP27 core set at various aspect ratios. The power handling of the structure scales with the aspect ratio (or volume) by changing the number of stacked core pieces in the center post and outer shell. Each curve also achieves a wide inductance range at its maximum power handling.

## 4.2 Approaches for Covering a Wide Range of Inductor Requirements

In this section, we explore the total achievable range of inductor requirements for two core sets. We show that there is a large overlap in achievable requirements between the MP27 core set and a core set with linear dimensions scaled equally to provide a factor-of-two scaling in volume. Due to this overlap, we show that a reasonable scaling of footprint size is a factor-of-four in volume to achieve a wide range of requirements with small overlap.

### 4.2.1 Factor-of-Two Volume Scaling

For typical industry-standard closed cores, e.g. RM or pot cores, sizes of adjacent cores scale roughly by a factor-of-two in volume [37,38]. Using this reference, we investigated the achievable range of a core set with each dimension scaled equally for a factor-of-two change in volume (MP33, see Table 4.1) and compared it to that of the MP27 core set. Fig. 4.4 shows a large overlap between the two core sets; the MP27 core set can achieve about 0.56 times the power handling of the MP33 core set.<sup>3</sup> In addition, at certain volumes (minimally between 1vol and 2vol, where vol is the volume of MP27 at  $h/D = 1$ ), the two cores have similar performance, despite having different aspect ratios and footprints. This comparable performance further highlights the overlap in achievable requirements; even at these fixed volumes, both core sets are equally favorable.

The negligible performance tradeoff between different aspect ratios at the same volume is reasonable within a certain range, as the  $Q$  of the structure falls off slowly from the optimum aspect ratio. At a volume of 1vol, the MP27 core set has an aspect ratio  $h/D = 1$ , while the MP33 core set has  $h/D = 0.5$ , which is not too far from the optimum aspect ratio of 1. At  $h/D = 0.5$ , the drop in  $Q$  is small enough that the increase in power dissipation can be compensated by the greater surface area of the structure.<sup>4</sup> Similarly, at

<sup>3</sup>This scaling can be predicted by the heat-flux-limited scaling factor  $\sim \epsilon^{2.6}$  in [2], which predicts a  $\sim 0.54$  scaling factor for a factor-of-two reduction in volume.

<sup>4</sup>For a cylinder, the minimum surface area for a given volume occurs at  $h/D = 1$ . Any shorter or taller aspect ratios at the

Table 4.1: Geometry of the MP17, MP27, MP33, and MP42 Core Sets

	MP17	MP27	MP33	MP42
Footprint Scale Factor (in vol)	0.25	1.0	2.0	4.0
Total Diameter ( $2r_t$ )	16.75 mm	26.9 mm	33.5 mm	42.2 mm
Centerpost Radius ( $r_c$ )	5.75 mm	9.9 mm	12.0 mm	15.5 mm
Window Width ( $w$ )	1.2 mm	1.4 mm	1.7 mm	2.1 mm
End Cap Height ( $h$ )	2.5 mm	4.0 mm	5.0 mm	6.0 mm
Core Piece Height	0.83 mm	1.18 mm	1.18 mm	1.46 mm

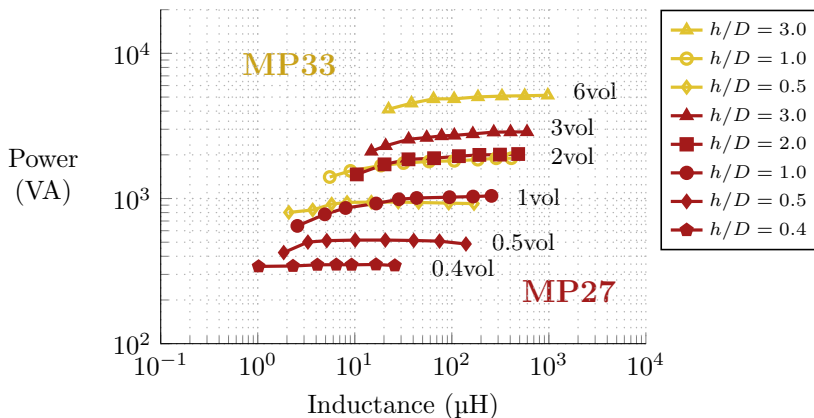


Figure 4.4: Maximum power handling curves at  $\Delta T = 40^\circ\text{C}$  of the MP27 (red) and MP33 (yellow) core sets at various aspect ratios. The two core sets have a large overlap in achievable inductor requirements. In particular, both core sets have comparable performance at the same volume but with different aspect ratios for volumes from 1vol to 2vol, where vol is the volume of MP27 at  $h/D = 1$ .

a volume of 2vol, the MP27 core set has  $h/D = 2$ , while the MP33 core set has  $h/D = 1$ . This comparable performance can be predicted by the  $Q$  versus aspect ratio graph (Fig 2.10), where the  $Q$  drops by at most 20% for aspect ratios between  $h/D = 0.5$  and  $h/d = 2.0$ .

## 4.2.2 Factor-of-Four Volume Scaling

With such a large overlap in achievable inductor requirements when scaling the MP27 core set by a factor-of-two in volume, we investigated scaling the core set by a factor-of-four in volume (MP42, see Table 4.1). Even with a factor-of-four scaling, there is still an overlap in performance between the two core sets at 2vol, where the MP27 core set has an aspect ratio of  $h/D = 2$  and the MP42 core set has  $h/D = 0.5$  (Fig. 4.5). At lower volumes, the MP42 core set has too short of an aspect ratio to maintain good performance, while at higher volumes, the MP27 core set is too tall.

Furthermore, we can confirm that the performance scales similarly with smaller core sets by comparing the MP27 core set with a core set scaled *down* by a factor-of-four in volume (MP17, see Table 4.1). Once again, both core sets cover wide ranges of inductances. The performance also overlaps when the aspect ratio of the larger MP27 core set is  $h/D = 0.5$  and the aspect ratio of the smaller MP17 core set is  $h/D = 2.0$  (Fig. 4.6).

---

same volume have greater surface area.

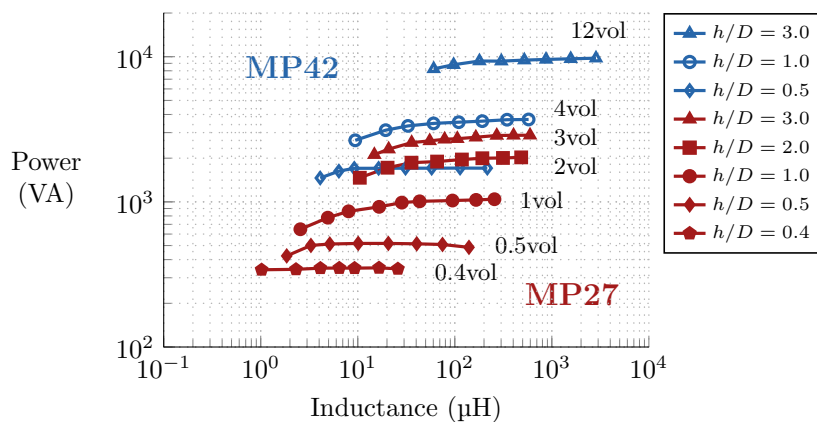


Figure 4.5: Maximum power handling curves at  $\Delta T = 40^\circ\text{C}$  of the MP27 (red) and MP42 (blue) core sets at various aspect ratios. The two core sets cover a wide range of inductor requirements, while still having an overlap in performance. In particular, both core sets have comparable performance at a volume of 2vol despite different aspect ratios, where vol is the volume of MP27 at  $h/D = 1$ .

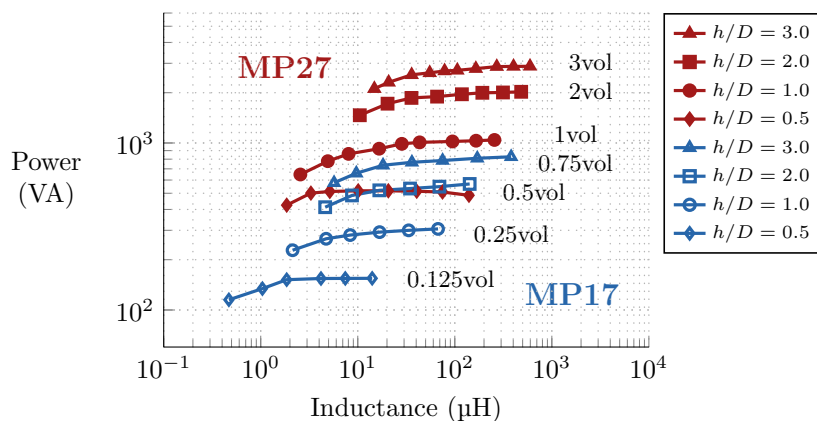


Figure 4.6: Maximum power handling curves at  $\Delta T = 40^\circ\text{C}$  of the MP17 (blue) and MP27 (red) core sets at various aspect ratios. Scaling down by a factor-of-four in volume scales performance similarly to scaling up by the same factor. The two core sets cover a wide range of inductor requirements, while still having an overlap in performance. In particular, both core sets have comparable performance at a volume of 0.5vol despite different aspect ratios, where vol is the volume of MP27 at  $h/D = 1$ .

When the aspect ratio of one core set deviates too much from a “square” aspect ratio, the performance between the two core sets differs. Decreasing the MP27 aspect ratio to  $h/D = 0.4$  to achieve a volume of 0.4vol results in much worse performance across a wide range of inductances compared to the same volume MP17 configuration. At very small inductances that require few turns, though, the  $h/D = 0.4$  MP27 can have comparable performance because a short and flat structure has better vertical window fill. Increasing the MP17 aspect ratio to  $h/D = 3.0$  at 0.75vol underperforms the MP27 configuration, except for large inductances with many turns that prefer larger window areas (Fig. 4.7).

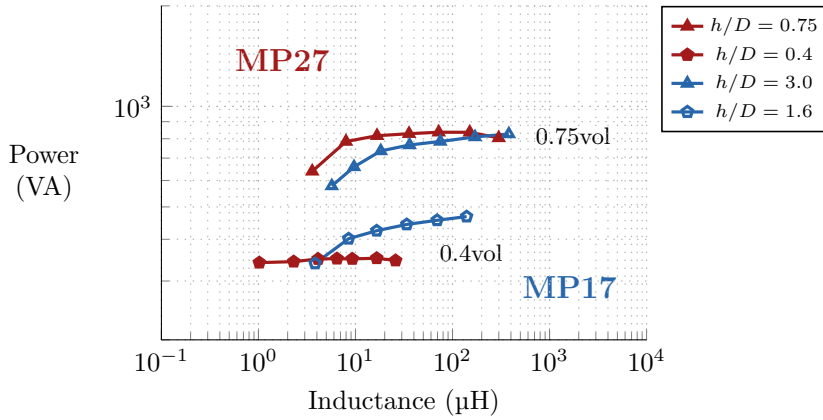


Figure 4.7: Maximum power handling curves at  $\Delta T = 40^\circ\text{C}$  of the MP17 (blue) and MP27 (red) core sets outside the overlap region. At small volumes, the short MP27 configuration at  $h/D = 0.4$  performs worse than the MP17 core set, while at large volumes, the tall MP17 configuration at  $h/D = 3.0$  performs worse than the MP27 core set. At very small and large inductances, however, the short MP27 aspect ratio and tall MP17 aspect ratio, respectively, can perform comparably to their same-volume counterparts.

As shown above, a factor-of-four volume scaling factor covers a wide range of inductor requirements, while maintaining a sufficient overlap in performance. This scaling factor can thus be a potential approach for achieving many different designs using a small set of components.





## Chapter 5

# Adapting the Proposed Structure for High-Power RF Applications

For high-power RF applications, design challenges for achieving low-loss inductors are amplified. At RF (13.56 MHz), skin effect has greater impact on winding loss due to the small skin depth (17.7  $\mu\text{m}$  for copper at 20 °C) at this frequency. (For reference, 40 AWG wire has a diameter of 79.9  $\mu\text{m}$ .) Core loss also increases significantly with frequency and can be difficult to keep low at high power. To circumvent high core losses, air-core inductors are traditionally used in high-power RF applications; however, recent development of high-performance core materials at HF has created an opportunity for high-power RF inductors with magnetic cores.

The low-loss design techniques from Chapter 2, namely quasi-distributed gaps and field shaping, can be extended to higher power levels and frequencies, allowing for cored inductor designs. This chapter presents a modified version of the proposed low-loss inductor structure, along with modified design guidelines, suitable for high-power RF applications, such as high-power RF amplifiers and matching networks for industrial plasma drive. With the modified structure and guidelines, an example 585 nH inductor achieved a  $Q$  of 1900 at 13.56 MHz and 78 A (peak, ac) in FEA simulation, thus demonstrating the potential of the design techniques to continue achieving low loss at high power and frequency.<sup>1</sup>

### 5.1 Modified Geometry for High-Power RF Applications

The modified proposed structure has a center post and end caps, but no outer shell (Fig. 5.1). For physically large inductors at high power, the outer shell no longer provides a good magnetic return path when designed to achieve double-sided conduction. Since the outer shell also contributes core loss, there is minimal benefit to having it in the structure; Section 5.2.1 discusses the design considerations for removing the outer shell in greater detail. The structure, however, still has a single-layer winding to reduce proximity-effect losses and quasi-distributed gaps to reduce fringing field effects. The single-layer winding is centered in the window with evenly spaced turns, and the quasi-distributed gaps are implemented with magnetically permeable discs separated by small gaps.

---

<sup>1</sup>This work was carried out in collaboration with Mr. Roderick Bayliss III, an MIT undergraduate.

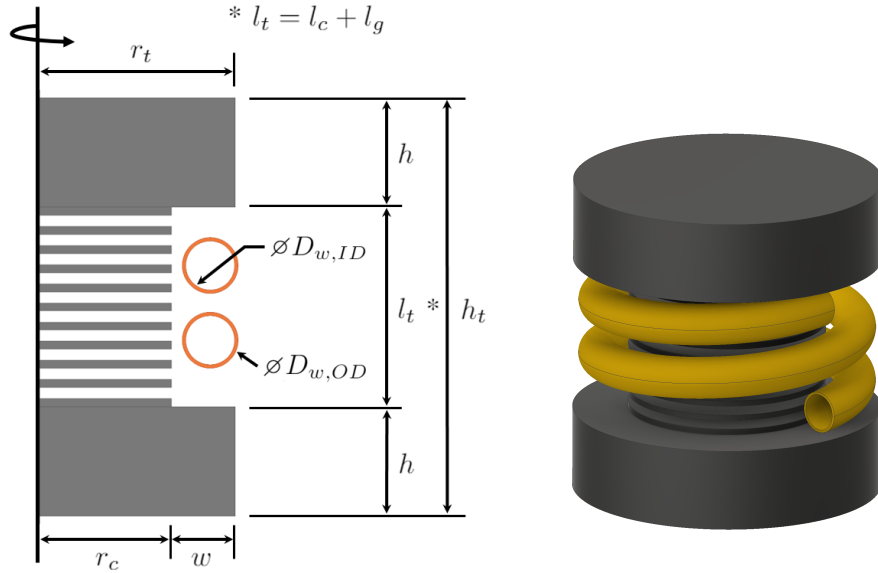


Figure 5.1: Radial cross-sectional view (left) of the modified proposed inductor, with only a center post and end caps. Parameters defining the geometry are labelled on this view as reference for Section 5.2. Revolving the cross-section about the axis of rotation produces the 3D model of the inductor on the right with a helical winding.

## 5.2 Changes in Design Guidelines

Operating in the high-power RF space introduces new design considerations. This section discusses the impact of these considerations on the design process of the original proposed structure and then presents modified design guidelines for the modified structure (Fig. 5.1).

### 5.2.1 Balance $H$ fields with the fringing field as the main flux return path to achieve double-sided conduction

As explained in Section 2.2.2, balancing the  $H$  fields on either side of a winding achieves double-sided conduction, where currents evenly distribute on both sides of the winding, and thus reduces winding loss. In the original proposed structure, balanced  $H$  fields are achieved by designing the center post and the return path to have equal reluctances, where the return path reluctance is composed of the outer shell reluctance in parallel with the fringing field reluctance. In this case, the outer shell reluctance dominates the return path, with the fringing field reluctance serving as a correction factor to achieve double-sided conduction. (For the example 16.6  $\mu\text{H}$  inductor in Chapter 3, the outer shell reluctance is 1.86 times greater than that of the fringing field reluctance, which translates to the outer shell containing about 65% of the flux.)

If we use the fringing field reluctance model derived from the air-core solenoid model in [28], valid for structures where  $h_t > \frac{2}{3}r_t$ , the fringing field reluctance is independent of the structure's height  $h_t$  and scales inversely with the radius  $r_t$ :

$$\mathcal{R}_f \approx \frac{0.9}{\mu_0 \pi r_t} \quad (5.1)$$

So, as the volume increases for a structure with a roughly “square” aspect ratio ( $h/D \approx 1$ ), the fringing field

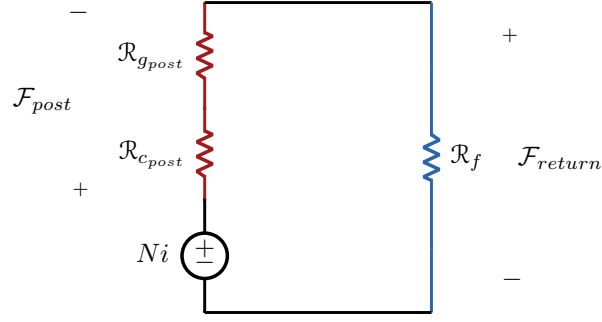


Figure 5.2: Magnetic circuit model used to balance the  $H$  fields in the modified proposed structure by making the reluctances of the center post (red) and fringing field return path (blue) equal. The discs of core material and the quasi-distributed gaps in the center post are treated as lumped reluctances. The end caps are composed of ungapped magnetic material and their reluctances are assumed to be negligible.

reluctance decreases.

At high power, a physically larger inductor is needed to handle the increase in power handling. With a larger radius, the inductor has a smaller fringing field reluctance that becomes the preferable flux return path compared to the outer shell. In addition, the outer shell adds core loss. With little benefit, the outer shell is no longer needed in physically large high-power inductors.

Getting rid of the outer shell means that the fringing field now serves as the main flux return path. To balance the  $H$  fields, the center post and outer shell reluctances should be the same (Fig. 5.2). Mathematically, we need

$$\mathcal{R}_{c_{post}} + \mathcal{R}_{g_{post}} = \mathcal{R}_f \quad (5.2)$$

where  $\mathcal{R}_{c_{post}}$  is the lumped reluctance of the discs of core material in the center post,  $\mathcal{R}_{g_{post}}$  is the lumped reluctance of the quasi-distributed gaps in the center post, and  $\mathcal{R}_f$  is the reluctance of the fringing path outside of the structure.

Neglecting local gap fringing,  $\mathcal{R}_{c_{post}}$  and  $\mathcal{R}_{g_{post}}$  can be calculated directly from the geometry (Fig. 5.1):

$$\mathcal{R}_{c_{post}} = \frac{l_c}{\mu_c \pi r_c^2} \quad (5.3)$$

$$\mathcal{R}_{g_{post}} = \frac{l_g}{\mu_0 \pi r_c^2} \quad (5.4)$$

where  $l_c$  is the combined height of the core material discs,  $l_g$  is the overall length of the gap, and  $\mu_c$  is the permeability of the core material.  $\mathcal{R}_f$  can be calculated using Eq. 5.1 or another fringing field reluctance model.

Having the fringing field as the main flux return path places an additional constraint on the proposed structure. For a desired inductance with a given number of turns, the total reluctance is set by:

$$\mathcal{R}_{total} = \mathcal{R}_{post} + \mathcal{R}_f = \frac{N^2}{L} \quad (5.5)$$

Since the center post and fringing field reluctances must be the same to achieve double-sided conduction ( $\mathcal{R}_{post} = \mathcal{R}_f$ ), the required fringing field reluctance is set at  $\mathcal{R}_f = \frac{N^2}{2L}$ , which in turn sets the total radius

$r_t$  of the structure. Therefore, for a desired inductance and number of turns, the modified structure needs a particular radius in order to achieve double-sided conduction.

Another way to view this constraint is to think about the effect of a fringing field return path on the achievable inductances for a given range of sizes. For a maximum desired volume at a single aspect ratio, there is a maximum total radius  $r_t$  and thus a minimum fringing field reluctance, which sets a maximum achievable inductance value. Lifting the aspect ratio constraint can extend the maximum achievable inductance, as shorter and flatter structures have larger radii. However, doing so has a practical limit since the  $Q$  of the structure drops significantly for structures with very low aspect ratios. So, even without a strict aspect ratio constraint, the modified structure has a maximum achievable inductance for a maximum desired volume.

### 5.2.2 Select a wire size that balances effective conduction area and parasitic capacitance

At high frequencies, the self-resonant frequency of an inductor may be near the frequency of operation and therefore, becomes an important design consideration [39, 40]. At (and near) self-resonance, additional circulating currents flow in the inductor due to self-coupling with its parasitic capacitance. These circulating currents increase loss and thus, degrade the inductor's quality factor. To push the self-resonant frequency further out and reduce the associated circulating currents, the parasitic capacitance of the inductor should be minimized. Two sources of such capacitance are the capacitive coupling within the winding and the capacitive coupling between the winding and the core [41]. Often, tackling the capacitive coupling within the winding is an easy and effective method to reduce the parasitic capacitance to a more manageable value. Increasing the space between turns in a winding reduces this coupling; this can be accomplished by spacing the turns as far apart as possible and decreasing the winding diameter.

Decreasing the winding diameter also helps to reduce proximity effect losses between turns. Doing so, however, reduces the available conduction area and thus increases winding loss. Therefore, the winding diameter should be chosen to balance the above effects to achieve a large effective conduction area in the winding while also reducing circulating currents due to self-resonance and proximity effects. To do so, an initial winding diameter should be chosen to maximize the horizontal window fill  $F_h$ ,<sup>2</sup> while ensuring that the turns physically fit in the height of the window. Then, the diameter should be incrementally decreased from this starting point to find the optimum  $Q$ .<sup>3</sup> The optimum diameter will likely occur at a horizontal window fill factor  $F_h$  close to 1; this value is larger than the recommended range from Section 2.2.5 since the modified structure only has gap fringing fields on one side of the window.

### 5.2.3 Aim for a copper-loss dominated design for easier thermal management

In general, the total loss of an inductor is usually minimized at a point where the core loss is close to, but slightly less than the copper loss. For a high-power RF inductor, a more copper-loss-dominated design may be preferable for easier thermal management, since heat can be more easily transferred from the exposed winding than the more densely packed core pieces. If the winding is constructed from copper tubing, as is commonly done for air-core inductors in this operating space, the winding can also be water-cooled. One possibility for cooling the core in the proposed structure is to use the non-magnetic spacers in the distributed

<sup>2</sup>The parasitic capacitance of the inductor as well as the initial  $Q$  that excludes self-resonant circulating currents can be found using FEA simulation. For a method to include the loss from the self-resonant effects in the  $Q$ , see Appendix H.

<sup>3</sup>For purposes of this design where we remove the outer shell, we define the horizontal fill factor as the fraction of the width between the center post and outer edge of the end cap which is utilized.

gap for heat extraction, such as by using thermally conductive (but ideally electrically isolating) materials in the spacer. This could include materials such as silicon nitride, for example.

### 5.3 An Example 585 nH Design

Using the modified structure and design guidelines, we designed an example 585 nH inductor that achieved a  $Q$  of 1900 at 13.56 MHz and 78 A (peak) of ac current in FEA simulation (Table 5.1). The example inductor was designed through an iterative process using a script.<sup>4</sup> First, a number of turns  $N$  was chosen, which set the radius  $r_t$  of the structure, and an end cap height  $h$  was chosen. Then, an initial outer winding diameter  $D_{w,OD}$  was chosen for a vertical window fill  $F_v$  between 50% and 80%, and a window width  $w$  was selected for a horizontal window fill  $F_h$  close to 1. The remaining parameters were calculated to balance the  $H$  fields for double-sided conduction. Adjustments to the core disc height  $l_c$  and gap length  $l_g$  from the script-generated values were made to more precisely tune the inductance of the design.

The above initial design was then iteratively refined. The height of the end caps was manually tuned for well-distributed  $B$  fields. The outer winding diameter was also tuned to minimize self-resonant circulating currents while still achieving high  $Q$ . Afterwards, the number of turns was tuned to achieve a design that was copper-loss-dominated for easier thermal management. Finally, the inner winding diameter  $D_{w,ID}$  was determined by the availability of copper tubing with the desired outer winding diameter (Table 5.2).

Table 5.1: Specifications for the simulated example RF inductor

Inductance	585 nH
Frequency	13.56 MHz
Current	78 A (peak, ac)
Core Material	Fair-Rite 67, $\mu_r = 40$ Steinmetz parameters: $k_c = 1.78 \times 10^{-9}$ , $\alpha = 2.20$ , $\beta = 2.12$ ( $P_v$ in mW/cm <sup>3</sup> , $f$ in MHz, $\hat{B}$ in mT)

Table 5.2: Geometry of the simulated example RF inductor (see Fig. 5.1)

Total Diameter ( $2r_t$ )	118.0 mm
Centerpost Radius ( $r_c$ )	37.8 mm
Total Height ( $h_t$ )	119.65 mm
End Cap Height ( $h$ )	31.3 mm
Total Core Length ( $l_c$ )	25.3 mm
Total Gap Length ( $l_g$ )	31.75 mm
Number of Turns ( $N$ )	2
Number of Gaps ( $N_g$ )	10
Wire Outer Diameter ( $D_{w,OD}$ )	16 mm
Wire Inner Diameter ( $D_{w,ID}$ )	14 mm

#### 5.3.1 Simulation Results

Simulation results verified that the example design achieved the desired low-loss features and thus had a high  $Q$ . The structure achieved low  $B$  fields for low core loss (Fig. 5.3a) and relatively balanced  $H$  fields (Fig. 5.3b) so that the winding had double-sided conduction (Fig. 5.4).

<sup>4</sup>For an example Python script, see Appendix I.

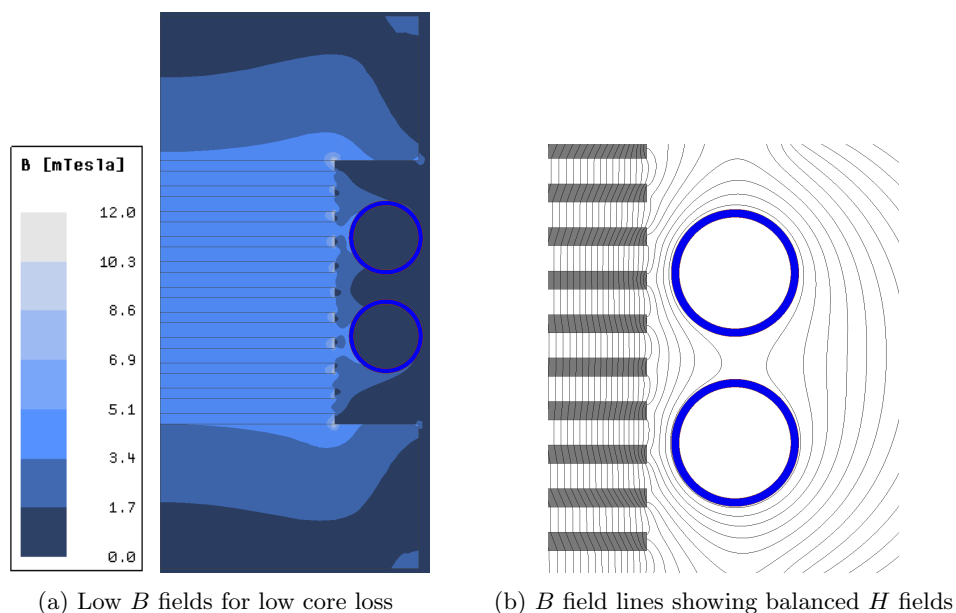


Figure 5.3:  $B$  field (blue),  $B$  field lines (black), and current distribution (rainbow) simulations of the example 585 nH inductor verifying that it achieves the desired low-loss features by following the design guidelines in Section 5.2. These 2D axisymmetric simulations capture one cross-section of the helical winding.

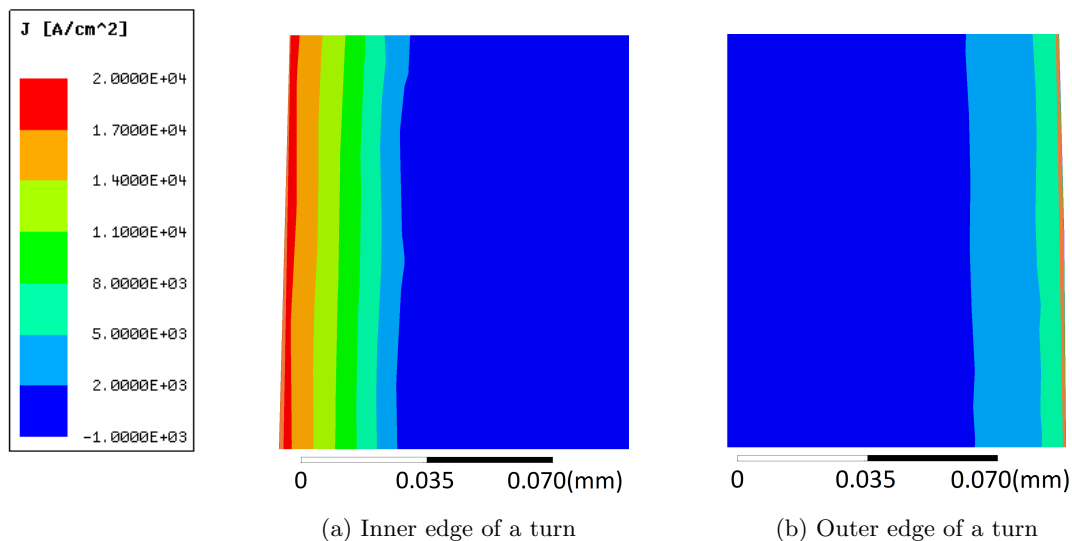


Figure 5.4: Current distribution (rainbow) simulations of the example 585 nH inductor verifying that its turns achieve (comparable) double-sided conduction by following the design guidelines in Section 5.2. The above figures are zoomed-in images of the inner and outer edge of one turn of the winding.

# Chapter 6

## Conclusion

### 6.1 Key Takeaways

Design of highly efficient, miniaturized inductors in the HF range is a significant challenge. The proposed inductor structure and design approach provide a solution for low-loss high-frequency power inductors. Using a set of analytic design guidelines, designers can achieve a roughly optimized inductor for a desired inductance and volume and then choose to further refine the design in FEA using the general design rules. This geometry and its guidelines for achieving high  $Q$  were confirmed experimentally through an example inductor with a manufactured  $Q$  of 720. In some cases, using litz wire with this geometry can improve its performance, and a  $Q$  of 980 was demonstrated with suitable litz wire, with experimental results aligning closely with simulation predictions.

The proposed structure also has great design and application flexibility. Many different structures can be constructed from a single core set by changing the number of stacked core pieces in the center post and outer shell. Thus, a wide range of inductor requirements can be achieved from a small set of core pieces. A possible approach to sizing core sets is to scale footprints by a factor-of-four in volume for large, continuous coverage of requirements. With this approach, the proposed structure and design techniques have greater potential for commercial adoption to facilitate the design of low-loss HF inductors.

Furthermore, the developed design techniques can be used in high-power RF applications to achieve low loss. In this operating space, a dumbbell-shaped core is preferred over a closed-core geometry for achieving double-sided conduction while maintaining low core loss. Associated design guidelines that roughly optimize the  $Q$  were also adapted from the original guidelines. Simulations of an example inductor support that the modified dumbbell geometry and guidelines can achieve high  $Q$  at high power and high frequency. The developed design techniques and proposed inductor structures are therefore suitable for achieving low-loss HF inductor designs for a potentially wide range of applications.

### 6.2 Future Work

This thesis largely focused on a single operation frequency (3 MHz), with some investigation into other frequencies in Sections 3.2.2 and 3.3.4 and Chapter 5. Further investigation of how the proposed structure performs across frequencies and at even higher frequencies would provide better understanding of the capabilities and limitations of the structure.

Another future direction might investigate how the double-sided conduction design technique developed in

this thesis may be applied in other situations. For example, application in planar magnetics (for integration with PCBs) and in transformers could be interesting to explore.

In addition to design techniques, manufacturing considerations are also important in the commercial adoption of research. While Appendix E provides construction methods of the proposed inductor structure for prototyping purposes, viable mass production processes need to be researched. A possible production process might include a stacking machine that alternates between gap and core materials. Another process might use a malleable gap material that is compressed to the desired height when stacking core pieces and then set once stacking is complete. For this research, communication with magnetics manufacturers would be key to understanding the needs and limitations of mass production processes.



## Appendix A

# Designing the Distributed Gap Geometry to Minimize Gap Fringing Loss

In this section, we show that setting the number of gaps  $N_g$  equal to the number of turns  $N$  aligns closely with the recommendation for minimizing gap fringing loss from [9], where the pitch between gaps ( $p$ ) should be less than four times the spacing between the gap and the conductor ( $s$ ), or  $p < 4s$ . We assume a large  $N$  so that the center-to-center spacing between each turn ( $p_w$ ) can be approximated as  $p_w = l_t/(N+1) \approx l_t/N$ , where  $l_t$  is the window height. Setting  $N_g = N$  also sets  $p = p_w$ , so the vertical and horizontal window fill are then

$$F_v = \frac{ND_w}{l_t} \approx \frac{D_w}{p} \quad (\text{A.1}) \quad F_h = \frac{D_w}{w} \quad (\text{A.2})$$

where  $D_w$  is the wire diameter and  $w$  is the window width (Fig. 2.1) Based on the geometry, the spacing between the gap and the winding is

$$s = \frac{w - D_w}{2} \quad (\text{A.3})$$

By combining (A.1)–(A.3), we get

$$\frac{p}{s} = \frac{2F_h}{F_v(1 - F_h)} \quad (\text{A.4})$$

Most combinations of  $F_v$  and  $F_h$  within the recommended ranges (Sections 2.2.4 and 2.2.5) satisfy the design criteria from [9],  $p < 4s$ . For example, for values in the center of these ranges,  $F_v = 0.65$  and  $F_h = 0.50$ ,  $p/s = 3.1 < 4$ . At the edge of these ranges where  $F_v$  is small and  $F_h$  is large, the  $p/s$  ratio surpasses the recommendation of  $p/s < 4$ , with the worst case at  $p/s = 6$ , when  $F_v = 0.50$  and  $F_h = 0.60$ . These edge cases, however, still achieve roughly optimal designs. Therefore, setting  $N_g = N$  yields designs for the proposed inductor that meet (or nearly meet) the design criterion of [9] and thus, achieve roughly optimum  $Q$ .

# Appendix B

## Simulation Details for Chapter 2

This section includes complete simulation details for relevant tables and plots from Chapter 2. These simulations were done in ANSYS Maxwell 2D Design, Versions 18.2 and 19.2. The windings for these simulations used the default ANSYS model for copper ( $\epsilon_r = 1$ ,  $\mu_r = 0.999991$ ,  $\sigma = 5.8 \times 10^{-7}$  S/m), and the inductors were simulated at 3 MHz and 2 A (peak, ac).

For simulations that used Fair-Rite 67 material ( $\mu_r = 40$ ), the following Steinmetz parameters were used to model core loss at 3 MHz:  $k_c = 0.034$ ,  $\alpha = 1.18$ , and  $\beta = 2.24$  ( $P_v$  in mW/cm<sup>3</sup>,  $f$  in MHz,  $\hat{B}$  in mT).

### B.1 Simulation and Geometry Details for Fig. 2.3

The example simulations for single-sided and double-sided conduction in Fig 2.3 were close-up views of the middle three turns of a winding on a rod-core inductor. Both simulations used the same inductor geometry with the winding vertically centered on the rod core (Table B.1) but with different core permeabilities. The single-sided conduction simulation had a high permeability of  $\mu_r = 1000$  for a lower  $H$  field on the inner side of the winding compared to the outer side. The double-sided conduction simulation had a low permeability of  $\mu_r = 10$  for balanced  $H$  fields on the inner and outer sides of the winding.

Table B.1: Geometry of the simulated rod-core inductors in Fig. 2.3

Rod Core Radius	1.5 mm
Rod Core Height	7.35 mm
Number of Turns	13
Winding Radius (to center of conductor)	1.84 mm
Wire Diameter	0.32 mm
Turn Spacing (center-to-center)	0.4 mm

### B.2 Simulation and Geometry Details for Fig. 2.5

The simulated proposed inductor in Fig. 2.5 is the same as the example 16.6  $\mu$ H design in Chapter 3; the geometry of this inductor is listed in Table 3.2. The simulated solenoid in this figure had roughly the same total height and radius as the simulated proposed inductor (Table B.2).

Table B.2: Geometry of the simulated solenoid in Fig. 2.5

Solenoid Radius (to center of conductor)	13.45 mm
Solenoid Height (conductor edge-to-edge)	26 mm
Number of Turns	13
Wire Diameter	0.8 mm
Turn Spacing (center-to-center)	2.1 mm

### B.3 Simulation and Geometry Details for Table 2.1

The geometries of the simulated inductors for Table 2.1 are presented in Table B.3. These inductors were designed for an inductance of 16.6  $\mu\text{H}$  at a volume of 14  $\text{cm}^3$ . The core material used for these inductors was Fair-Rite 67. These inductors were not optimized for  $Q$ , as they were only intended to validate the fringing field reluctance model (Section 2.2.2).

Table B.3: Geometry of the simulated inductors in Table 2.1

Aspect Ratio ( $h/(2r_t)$ )	0.33	0.5	1.0	1.5	2.0
Total Diameter ( $2r_t$ )	37.674 mm	32.912 mm	26.122 mm	22.82 mm	20.734 mm
Centerpost Radius ( $r_c$ )	14.485 mm	12.396 mm	8.98 mm	7.166 mm	6.278 mm
Window Width ( $w$ )	0.79 mm	0.781 mm	1.673 mm	2.422 mm	2.678 mm
Total Height ( $h_t$ )	12.56 mm	16.453 mm	26.122 mm	34.234 mm	41.473 mm
End Cap Height ( $h$ )	2.0 mm	4.0 mm	4.0 mm	4.0 mm	4.0 mm
Total Core Length ( $l_c$ )	4.452 mm	5.502 mm	16.926 mm	25.844 mm	33.248 mm
Total Gap Length ( $l_g$ )	4.108 mm	2.951 mm	1.196 mm	0.39 mm	0.225 mm
Number of Turns ( $N$ )	13	13	13	13	15
Number of Gaps ( $N_g$ )	13	13	13	13	15
Wire Diameter ( $D_w$ )	0.394 mm	0.390 mm	0.836 mm	1.210 mm	1.338 mm

### B.4 Simulation and Geometry Details for Fig. 2.7

In Fig. 2.7, a range of vertical window fills  $F_v$  was simulated for three different core geometries with the same volume (14.4  $\text{cm}^3$ ) but different window heights  $l_t = \{14.3 \text{ mm}, 18.3 \text{ mm}, 22.3 \text{ mm}\}$ . Table B.4 lists dimensions for the three core geometries, and Table B.5 lists the winding diameters used to achieve the desired range of vertical window fills for each window height. The inductors all had the same inductance of 16.1  $\mu\text{H}$  and used Fair-Rite 67 for the core material.

Table B.4: Core geometry for the simulations in Fig. 2.7 at different window heights  $l_t$ 

Window Height ( $l_t$ )	14.3 mm	18.3 mm	22.3 mm
Total Diameter ( $2r_t$ )	26.298 mm	26.298 mm	26.298 mm
Centerpost Radius ( $r_c$ )	6.106 mm	6.106 mm	6.106 mm
Window Width ( $w$ )	6.0 mm	6.0 mm	6.0 mm
Total Height ( $h_t$ )	26.3 mm	26.303 mm	26.311 mm
End Cap Height ( $h$ )	6.0 mm	4.0 mm	2.0 mm
Total Core Length ( $l_c$ )	13.832 mm	18.004 mm	22.246 mm
Total Gap Length ( $l_g$ )	0.468 mm	0.299 mm	0.065 mm
Number of Turns ( $N$ )	13	13	13
Number of Gaps ( $N_g$ )	13	13	13

Table B.5: Wire diameters for a range of vertical window fills at different window heights

Vertical Fill ( $F_v$ )	Wire Diameter ( $D_w$ ) for $l_t = 14.3$ mm	Wire Diameter ( $D_w$ ) for $l_t = 18.3$ mm	Wire Diameter ( $D_w$ ) for $l_t = 22.3$ mm
0.3	0.33 mm	0.40 mm	0.53 mm
0.4	0.44 mm	0.55 mm	0.70 mm
0.5	0.55 mm	0.70 mm	0.87 mm
0.6	0.66 mm	0.85 mm	1.04 mm
0.7	0.77 mm	1.00 mm	1.21 mm
0.8	0.88 mm	1.15 mm	1.38 mm
0.9	0.99 mm	1.30 mm	1.55 mm

## B.5 Simulation and Geometry Details for Fig. 2.9

In Fig. 2.9, a range of horizontal window fills  $F_h$  was simulated for five different core geometries with the same volume ( $14.4 \text{ cm}^3$ ) but different window widths  $w = \{1.00 \text{ mm}, 1.50 \text{ mm}, 1.75 \text{ mm}, 2.00 \text{ mm}, 3.17 \text{ mm}\}$ . Each core geometry had the same number of turns ( $N = 13$ ) but different winding diameters  $D_w = \{0.7 \text{ mm}, 0.9 \text{ mm}, 1.1 \text{ mm}\}$  to achieve different vertical window fills  $F_v = \{50\%, 64\%, 78\%\}$ , respectively. The inductors all had the same inductance of  $16.5 \mu\text{H}$  and used Fair-Rite 67 for the core material. Table B.6 lists dimensions for the five core geometries, and Table B.7 provides the achieved  $F_h$  for each combination of winding diameter and window width.

Table B.6: Core geometry for the simulations in Fig. 2.9 at different window widths

Window Width ( $w$ )	1.00 mm	1.50 mm	1.75 mm	2.00 mm	3.17 mm
Total Diameter ( $2r_t$ )	26.3 mm	26.3 mm	26.3 mm	26.3 mm	26.3 mm
Centerpost Radius ( $r_c$ )	9.5 mm	9.19 mm	9.03 mm	8.875 mm	8.11 mm
Total Height ( $h_t$ )	26.311 mm	26.307 mm	26.312 mm	26.303 mm	26.31 mm
End Cap Height ( $h$ )	4.0 mm	4.0 mm	4.0 mm	4.0 mm	4.0 mm
Total Core Length ( $l_c$ )	16.842 mm	16.968 mm	17.038 mm	17.094 mm	17.374 mm
Total Gap Length ( $l_g$ )	1.469 mm	1.339 mm	1.274 mm	1.209 mm	0.936 mm
Number of Turns ( $N$ )	13	13	13	13	13
Number of Gaps ( $N_g$ )	13	13	13	13	13

Table B.7: Combinations of wire diameters  $D_w$  and window widths  $w$  to achieve a range of horizontal window fills  $F_h$  at different vertical window fills  $F_v$ 

	$D_w = 0.7$ mm ( $F_v = 50\%$ )	$D_w = 0.9$ mm ( $F_v = 64\%$ )	$D_w = 1.1$ mm ( $F_v = 78\%$ )
$w = 1.00$ mm	$F_h = 22\%$	$F_h = 28\%$	$F_h = 35\%$
$w = 1.50$ mm	$F_h = 35\%$	$F_h = 45\%$	$F_h = 44\%$
$w = 1.75$ mm	$F_h = 40\%$	$F_h = 51\%$	$F_h = 55\%$
$w = 2.00$ mm	$F_h = 47\%$	$F_h = 60\%$	$F_h = 63\%$
$w = 3.17$ mm	$F_h = 70\%$	$F_h = 90\%$	$F_h = 73\%$

## B.6 Simulation and Geometry Details for Fig. 2.10

In Fig. 2.10, inductors with a range of different height-to-diameter aspect ratios ( $h/D$ ) were simulated at three different volumes ( $7\text{ cm}^3$ ,  $14\text{ cm}^3$ ,  $28\text{ cm}^3$ ). For each inductor, all geometric parameters, except for the aspect ratio, were designed using the guidelines from Section 2.2. The inductors had the same inductance ( $16.6\text{ }\mu\text{H}$ ) and used Fair-Rite 56 for the core material. Tables B.8, B.9, and B.10 list geometry details for the simulated inductors with different aspect ratios at volumes of  $7\text{ cm}^3$ ,  $14\text{ cm}^3$ , and  $28\text{ cm}^3$ , respectively.

Table B.8: Geometries for simulated inductors with different aspect ratios at a volume of  $7\text{ cm}^3$  from Fig. 2.10

Aspect Ratio ( $h/D$ )	0.33	0.67	1.0
Total Diameter ( $2r_t$ )	29.902 mm	23.734 mm	20.734 mm
Centerpost Radius ( $r_c$ )	10.658 mm	8.401 mm	7.303 mm
Window Width ( $w$ )	0.663 mm	0.882 mm	1.098 mm
Total Height ( $h_t$ )	9.989 mm	15.821 mm	20.73 mm
End Cap Height ( $h$ )	2.5 mm	3.5 mm	3.5 mm
Total Core Length ( $l_c$ )	4.17 mm	7.813 mm	12.56 mm
Total Gap Length ( $l_g$ )	0.819 mm	1.008 mm	1.17 mm
Number of Turns ( $N$ )	9	12	15
Number of Gaps ( $N_g$ )	9	12	15
Wire Diameter ( $D_w$ )	0.331 mm	0.442 mm	0.55 mm

Aspect Ratio ( $h/D$ )	1.33	2.0	4.0
Total Diameter ( $2r_t$ )	18.838 mm	16.456 mm	13.061 mm
Centerpost Radius ( $r_c$ )	6.675 mm	5.787 mm	4.508 mm
Window Width ( $w$ )	1.208 mm	1.413 mm	1.752 mm
Total Height ( $h_t$ )	25.096 mm	32.885 mm	52.211 mm
End Cap Height ( $h$ )	3.5 mm	3.5 mm	3.5 mm
Total Core Length ( $l_c$ )	16.53 mm	24.081 mm	43.072 mm
Total Gap Length ( $l_g$ )	1.566 mm	1.804 mm	2.139 mm
Number of Turns ( $N$ )	18	22	31
Number of Gaps ( $N_g$ )	18	22	31
Wire Diameter ( $D_w$ )	0.604 mm	0.706 mm	0.876 mm

Table B.9: Geometries for simulated inductors with different aspect ratios at a volume of  $14 \text{ cm}^3$  from Fig. 2.10

Aspect Ratio ( $h/D$ )	0.33	0.67	1.0
Total Diameter ( $2r_t$ )	37.942 mm	30.114 mm	26.3 mm
Centerpost Radius ( $r_c$ )	13.626 mm	10.815 mm	9.475 mm
Window Width ( $w$ )	0.697 mm	1.207 mm	1.465 mm
Total Height ( $h_t$ )	12.671 mm	20.081 mm	26.303 mm
End Cap Height ( $h$ )	4.0 mm	4.0 mm	4.0 mm
Total Core Length ( $l_c$ )	3.447 mm	10.257 mm	16.128 mm
Total Gap Length ( $l_g$ )	1.224 mm	1.824 mm	2.175 mm
Number of Turns ( $N$ )	8	12	15
Number of Gaps ( $N_g$ )	8	12	15
Wire Diameter ( $D_w$ )	0.348 mm	0.604 mm	0.732 mm

Aspect Ratio ( $h/D$ )	1.33	2.0	4.0
Total Diameter ( $2r_t$ )	23.902 mm	20.88 mm	16.572 mm
Centerpost Radius ( $r_c$ )	8.536 mm	7.473 mm	5.784 mm
Window Width ( $w$ )	1.685 mm	1.929 mm	2.412 mm
Total Height ( $h_t$ )	31.855 mm	41.719 mm	66.238 mm
End Cap Height ( $h$ )	4.0 mm	4.0 mm	4.0 mm
Total Core Length ( $l_c$ )	21.492 mm	30.8 mm	54.99 mm
Total Gap Length ( $l_g$ )	2.363 mm	2.919 mm	3.248 mm
Number of Turns ( $N$ )	17	21	29
Number of Gaps ( $N_g$ )	17	21	29
Wire Diameter ( $D_w$ )	0.842 mm	0.964 mm	1.206 mm

Table B.10: Geometries for simulated inductors with different aspect ratios at a volume of  $28 \text{ cm}^3$  from Fig. 2.10

Aspect Ratio ( $h/D$ )	0.33	0.67	1.0
Total Diameter ( $2r_t$ )	47.468 mm	37.674 mm	32.912 mm
Centerpost Radius ( $r_c$ )	16.946 mm	13.392 mm	11.778 mm
Window Width ( $w$ )	1.323 mm	1.758 mm	2.05 mm
Total Height ( $h_t$ )	15.84 mm	25.1 mm	32.882 mm
End Cap Height ( $h$ )	3.5 mm	4.5 mm	4.5 mm
Total Core Length ( $l_c$ )	6.984 mm	13.68 mm	20.76 mm
Total Gap Length ( $l_g$ )	1.856 mm	2.42 mm	3.122 mm
Number of Turns ( $N$ )	8	11	14
Number of Gaps ( $N_g$ )	8	11	14
Wire Diameter ( $D_w$ )	0.662 mm	0.879 mm	1.024 mm

Aspect Ratio ( $h/D$ )	1.33	2.0	4.0
Total Diameter ( $2r_t$ )	29.902 mm	26.122 mm	20.734 mm
Centerpost Radius ( $r_c$ )	10.342 mm	9.081 mm	6.789 mm
Window Width ( $w$ )	2.47 mm	2.731 mm	3.412 mm
Total Height ( $h_t$ )	39.835 mm	52.207 mm	82.874 mm
End Cap Height ( $h$ )	4.5 mm	4.5 mm	4.5 mm
Total Core Length ( $l_c$ )	28.24 mm	39.92 mm	70.416 mm
Total Gap Length ( $l_g$ )	2.595 mm	3.287 mm	2.458 mm
Number of Turns ( $N$ )	15	19	26
Number of Gaps ( $N_g$ )	15	19	26
Wire Diameter ( $D_w$ )	1.234 mm	1.366 mm	1.706 mm

## Appendix C

### First-Order Derivation of Loss in the Active Section

In this section, we quantitatively show to first-order that the loss of the active section of the structure (everything within  $l_t$ ) decreases as the diameter increases. To do this, we consider the equivalent resistance of the active section.

The winding resistance is

$$R_w = \rho N \frac{2\pi r_c}{A_1} = \rho k_w N^2 \frac{2\pi r_c}{l_t} \quad (\text{C.1})$$

where it is assumed that the available conduction area of a turn  $A_1$  is proportional to the area of the window with the proportionality constant  $1/k_w$ , i.e.  $A_1 = l_t/(k_w N)$ , and the radius of the winding path is approximated as the center post radius  $r_c$ .

For the equivalent resistance of the core loss in the active section, we consider only the center post core loss for simplicity, since the outer shell core loss is on the same order. The core loss in the center post is given by

$$\begin{aligned} P_{core} &= k_c (l_t \pi r_c^2) \times \hat{B}^\beta = k_c (l_t \pi r_c^2) \times \left( \frac{LI_{pk}}{N\pi r_c^2} \right)^\beta \\ &\approx k_c (l_t \pi r_c^2) \times \left( \frac{LI_{pk}}{N\pi r_c^2} \right)^2 \end{aligned} \quad (\text{C.2})$$

where we approximate  $\beta = 2$  (not uncommon for low frequencies; usually an under-estimate at high frequencies). We may then express core loss through an equivalent resistance,

$$R_{core} = P_{core}/I_{rms}^2 = 2k_c l_t \frac{L^2}{N^2 \pi r_c^2} \quad (\text{C.3})$$

In an optimized design, core loss is approximately equal to winding loss. Equating the resistances yields

$$N_{opt} = \left( \frac{k_c l_t^2 L^2}{\rho k_w \pi^2 r_c^3} \right)^{1/4} \quad (\text{C.4})$$

$$R_w = R_{core} = \rho k_w N_{opt}^2 \frac{2\pi r_c}{l_t} = 2L \sqrt{\frac{\rho k_w k_c}{r_c}} \propto \sqrt{\frac{1}{r_c}} \quad (\text{C.5})$$

so that the total equivalent resistance of the active section is proportional to  $\sqrt{1/r_c}$ . Thus, the loss in this section decreases as diameter increases.

## Appendix D

### Example Python Script for Automating Initial Designs of the Proposed Structure

```
#####  
# Example python script for automating the design process of the inductor geometry  
# proposed in "A Low-Loss Inductor Structure and Design Guidelines for  
# High-Frequency Applications"  
# (R. S. Yang, A. J. Hanson, B. A. Reese, C. R. Sullivan, and D. J. Perreault)  
#  
# Notes:  
# See Fig. 2.11 in Chapter 2 for a flowchart of the design process  
# Compatibility with both Python 2 & 3  
#  
# Date last modified: 11.06.2018  
#####  
  
# libraries  
from __future__ import print_function # for compatibility with both Python 2 & 3  
import math  
  
# constants  
u0 = 1.257e-6 # permeability of free space in [H/m]  
Fv = 0.6 # vertical fill factor of winding in window  
# (can range from 0 to 1, recommended range from 0.5 to 0.8)  
Fh = 0.5 # horizontal fill factor of winding in window  
# (can range from 0 to 1, recommended range from 0.4 to 0.6)  
ratio = 1.0 # aspect ratio (defined as height/diameter) (optimized at 1.0)  
  
# input variables  
uc = 40. # relative permeability of core material  
L = 16e-6 # desired inductance in [H]  
vol = 14.77e-6 # desired volume in [m^3]  
N = 13. # number of turns  
h = 0.004 # height of end cap in [m]  
  
if __name__ == '__main__':  
    # set number of gaps (Ng) equal to the number of turns (N) (Appendix A)  
    Ng = N
```



```

# compute total radius (rt) and total height (ht) from volume and aspect ratio
# (ratio) (Sec. 2.2.6)
rt = ( (vol/ratio)/(2*math.pi) )**(1./3.)
ht = 2*rt*ratio

# compute wire diameter (Dw) to achieve desired vertical window fill (Fv)
# (Sec. 2.2.4)
Dw = (ht - 2.*h) * Fv / N

# computer window width (w) to achieve desired horizontal window fill (Fh)
# (Sec. 2.2.5)
w = Dw / Fh

# compute overall fringing field reluctance (Rf) of the structure (Sec. 2.2.2)
# NOTE: here, we use Eq. 8 in the paper, which derives Rf from the air-core
# solenoid model found in:
# T. H. Lee, Planar Microwave Engineering: A Practical Guide to Theory,
# Measurement, and Circuits, 1st ed., Cambridge University Press, 2004,
# pp. 140–142.
Rf = .9 / (u0*math.pi*rt)

# compute radius of center post (rc), total core length (lc), and total gap
# length (lg) using the calculated Rf to achieve equal reluctances in the
# center post and return path for balanced H fields (Sec. 2.2.2)
rc = (2*L*Rf*w - math.sqrt(4*(L*Rf*w)**2 - 2*L*Rf*(rt**2 - w**2)*(N**2 - 4*L*Rf)))/(N**2
- 4*L*Rf)
lc = (N**2/(2*L) * u0*math.pi*rc**2 - ht + 2*h) / (1/uc - 1.)
lg = ht - lc - 2*h

# print out computed geometric parameters
print("")
print("GEOMETRIC PARAMETERS FOR L = ", L, "H, volume = ", vol, "m^3")
print("")

print("total radius:\t\t\t rt = ", rt * 1000, "mm")
print("\t centerpost radius:\t rc = ", rc * 1000, "mm")
print("\t window width:\t\t w = ", w * 1000, "mm")

print("total height:\t\t\t ht = ", ht * 1000, "mm")
print("\t end cap height:\t h = ", h * 1000, "mm")
print("\t total core length:\t lc = ", lc * 1000, "mm")
print("\t total gap length:\t lg = ", lg * 1000, "mm")

print("number of turns:\t\t N = ", N)
print("number of gaps:\t\t Ng = ", Ng)
print("wire diameter:\t\t\t Dw = ", Dw * 1000, "mm")

```

# Appendix E

## Prototype Construction

In this section, we provide fabrication details of the prototype inductor from Section 3.2.1 for those interested in prototyping processes. The construction methods below are not intended as a viable mass production process. All magnetic core pieces were custom manufactured by Fair-Rite Products Corp.

### E.1 Prototype Construction of the Example 16.6 $\mu\text{H}$ Design

The prototype inductor was constructed modularly with the aid of custom 3D-printed fixtures. The center post was constructed first (Fig. E.1a) with one of the end caps. To control the quasi-distributed gaps, we stacked laser cut pieces of polyester plastic shimstock<sup>1</sup> with the appropriate thickness (0.114 mm) in between each layer of core material. To center all of the center post layers, a 1 mm-diameter hole was drilled in the center of the discs and the center post shimstock pieces so they could be assembled on a rod. Since the drilled holes were relatively small, we expect minimal effect on the fields.

For the winding, 20 AWG solid core wire with Teflon fluorinated ethylene propylene (FEP)<sup>2</sup> insulation was wound around a 3D-printed fixture of the same diameter as the center post (Fig. E.1b). The wire was chosen to have the appropriate insulation thickness (0.229 mm from the conductor diameter to the outer diameter) to center it in the window. Then, the winding was wrapped in a single layer of 0.079 mm thick polypropylene tape (package sealing tape) to maintain its shape, removed from the fixture and put on the center post.

The outer shell, composed of three sections to allow for vertical windows (with approximate widths of 1.5 mm), was constructed one section at a time. Each section was stacked on a 3D-printed fixture, alternating between layers of core material and laser cut shimstock (Fig. E.1c). The outer surface of each section was taped to hold all the pieces together. Then, the sections were added to the center post structure so that the two winding terminations could leave the structure through one of the vertical windows in the shell.

Afterwards, the second end cap was added, and the rod was removed from the centerpost. Finally, the entire circumference of the inductor was wrapped with a single layer of package sealing tape to apply radial pressure, and a strip of package sealing tape was wrapped vertically around the inductor to apply vertical pressure.

---

<sup>1</sup>Each gap was composed of two shimstock pieces of different thicknesses stacked together to get the desired 0.114 mm thickness. The two thicknesses were:  $0.003'' \pm 0.0002''$  and  $0.0015'' \pm 0.0002''$ .

<sup>2</sup>Teflon insulation was chosen for its low dielectric loss, which was particularly important in this prototype due to the winding's rather thick insulation. Insulation material with greater dielectric loss (e.g. polyurethane commonly found on magnet wire) may still provide negligible loss in windings with thinner insulation.

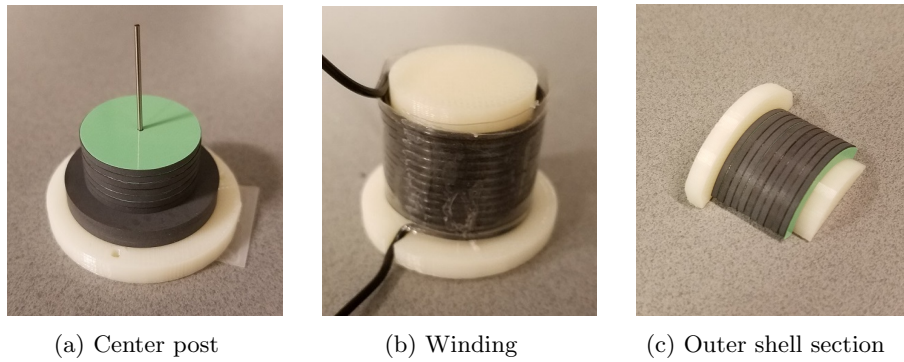


Figure E.1: Construction of the prototype inductor using custom 3D-printed fixtures (white).

## E.2 CAD Drawings for the Manufactured Core Pieces

Below are CAD drawings for the three types of manufactured core pieces for the prototype in Chapter 3.

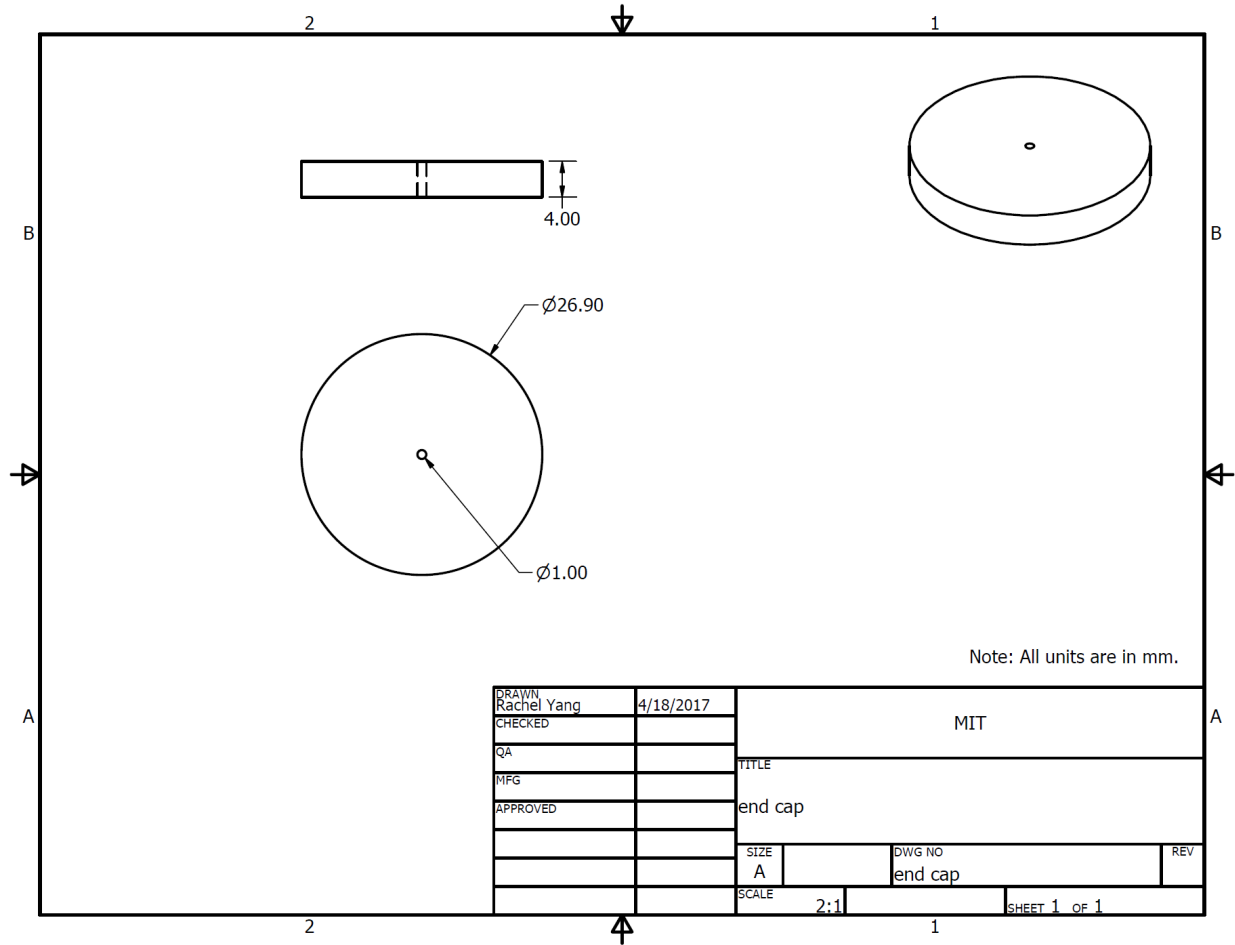


Figure E.2: CAD drawing of the manufactured end cap part

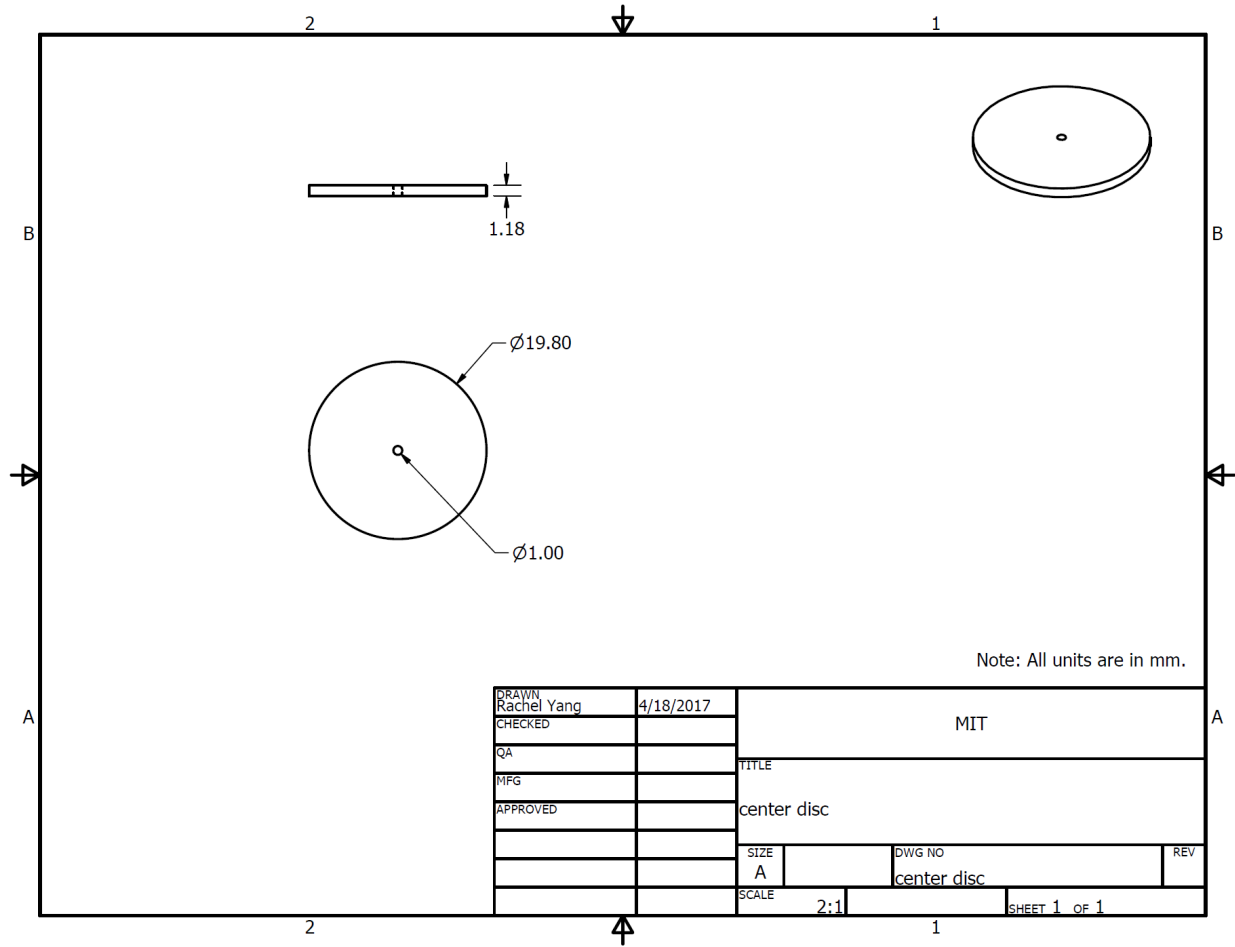


Figure E.3: CAD drawing of the manufactured core disc part for the center post

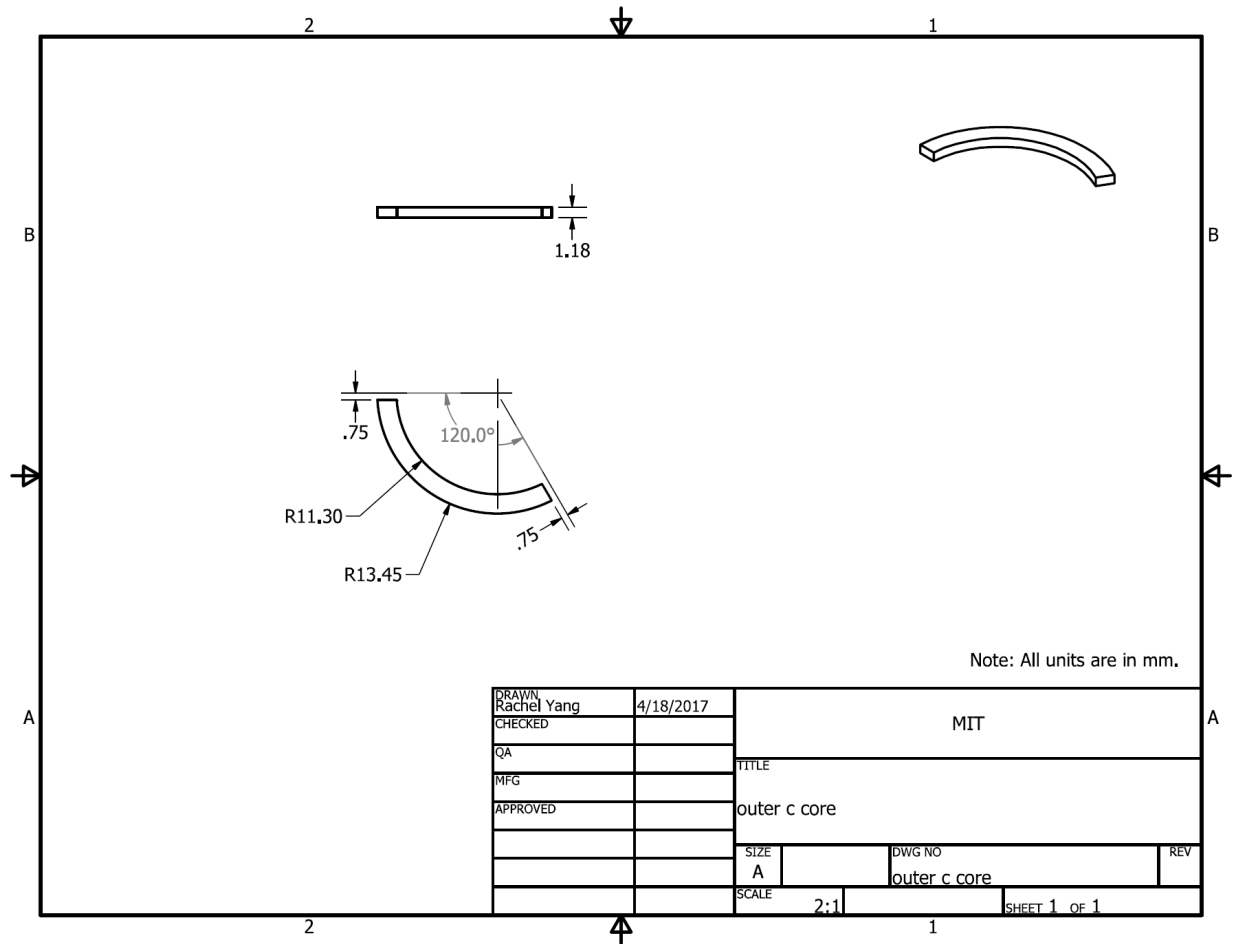


Figure E.4: CAD drawing of the manufactured outer shell section

### E.3 CAD Drawings for the 3D-printed Fixtures

Below are CAD drawings for the custom 3D-printed fixtures used in prototype construction (Section E.1).

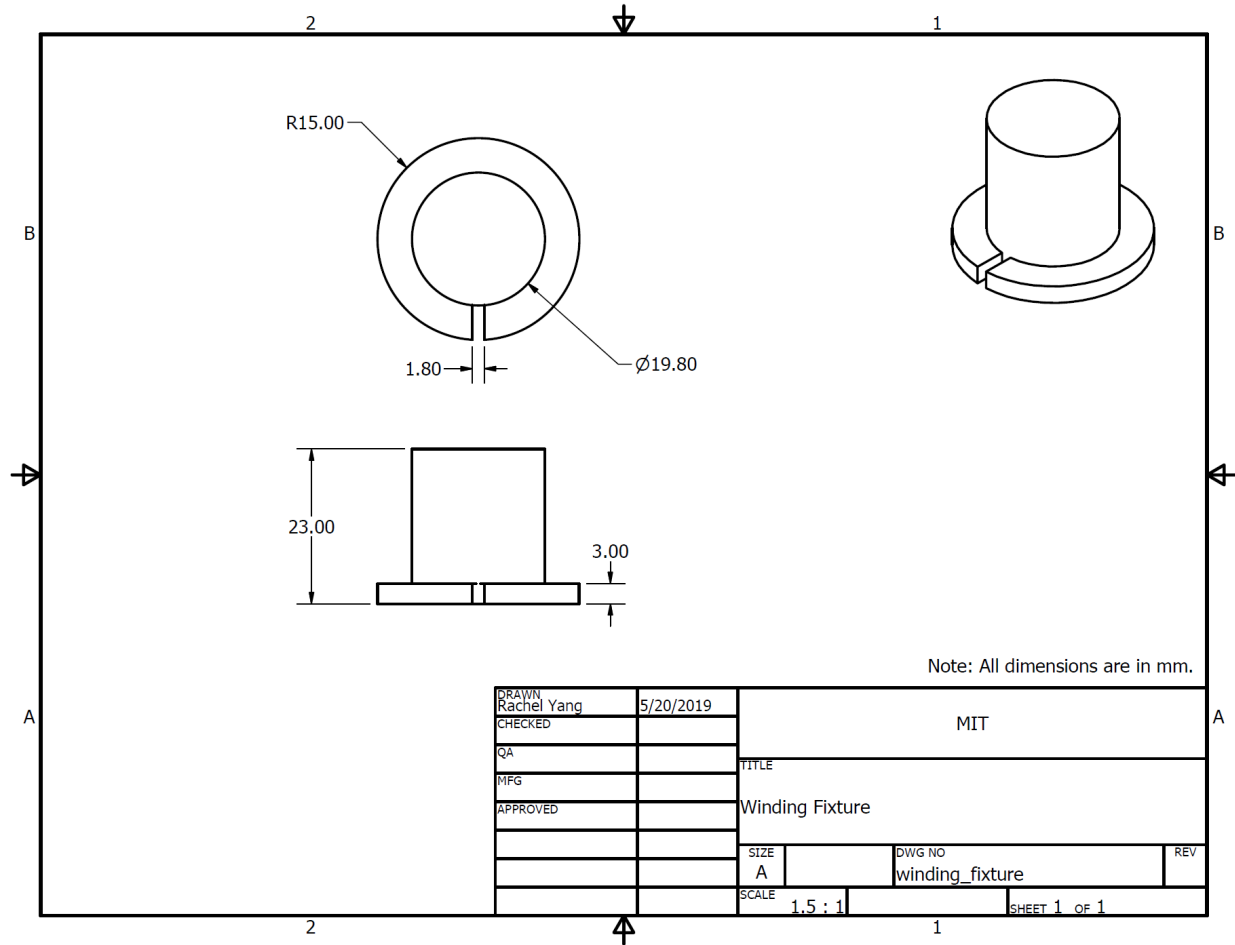


Figure E.5: CAD drawing of the custom 3D-printed fixture for the winding (see Fig. E.1b)

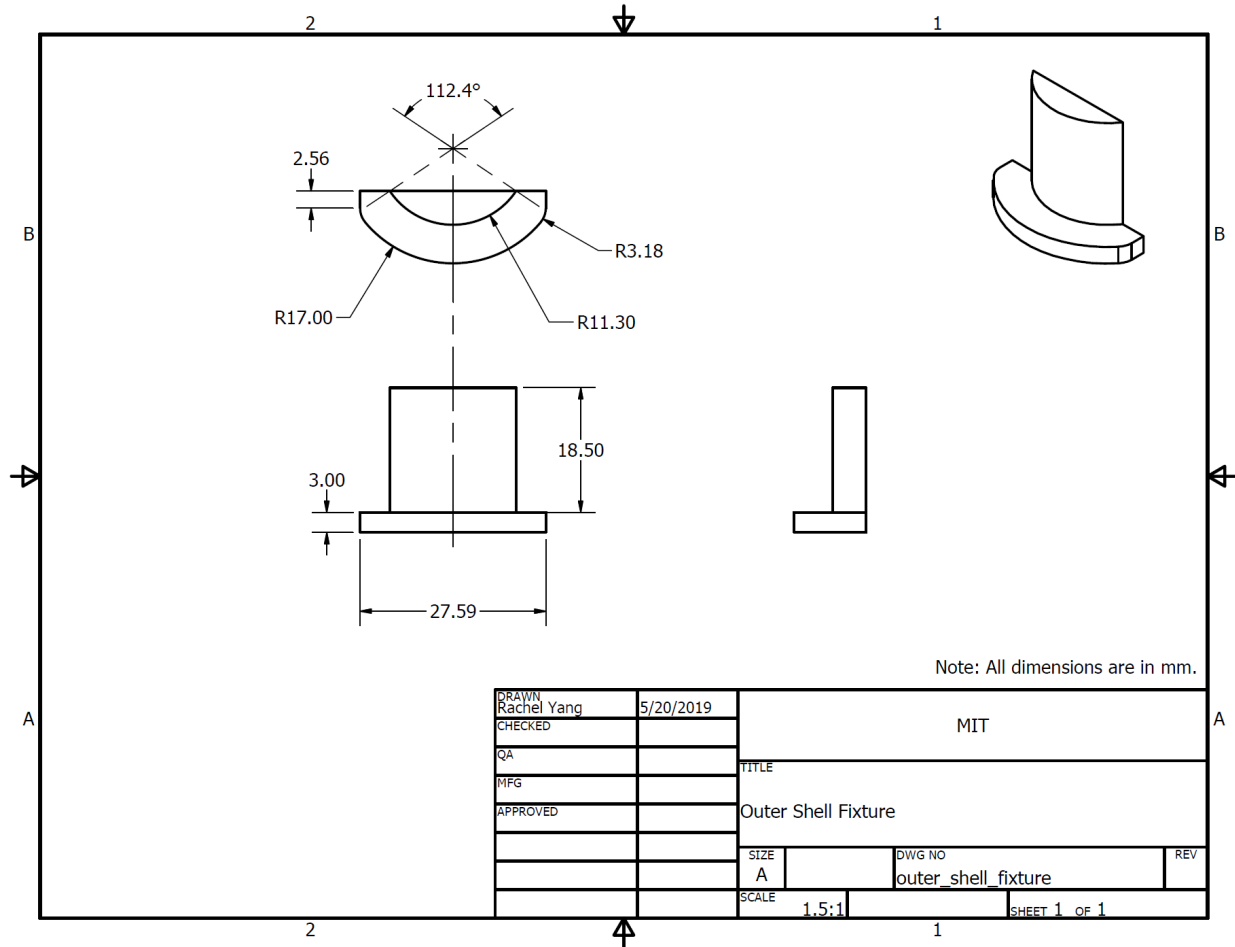


Figure E.6: CAD drawing of the custom 3D-printed fixture for assembling the outer shell sections (see Fig. E.1c)



## Appendix F

### Measuring High $Q$ (large-signal)

To measure the large-signal  $Q$  of the prototype inductors, we used the same resonant measurement approach from [11] and [12] and added some modifications for measuring high  $Q$ . The original approach operates a series LC circuit at resonance so that the ratio of the peak capacitor voltage to the peak input voltage can be approximated as the  $Q$  of the inductor. When measuring a high  $Q$ , though, several assumptions in this approach no longer hold, leading to two modifications. Below, we discuss these modifications and other considerations for high- $Q$  measurements at high frequency. We also show the validation of this modified measurement approach with an air-core inductor.

#### F.1 Use a capacitor divider to minimize probe loss and loading

When measuring a high- $Q$  inductor, we expect a high resonant capacitor voltage. The probe loss and loading at this high-frequency, high-voltage node, however, can significantly affect results. To get a more accurate measurement of the resonant capacitor voltage, we replaced the capacitor in the original approach with a capacitor divider having the same net impedance. The stepped-down voltage can then be measured with minimal probe loss and loading (Fig. F.1).

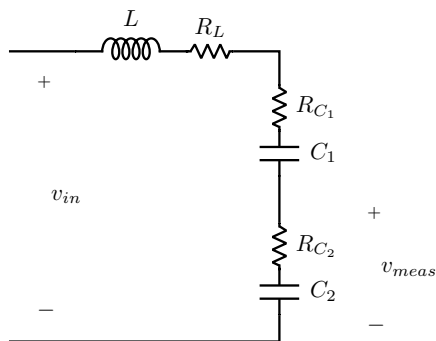


Figure F.1: Circuit for the resonant measurement approach to measure high  $Q$ , modified to include a capacitor divider to step down the measured output voltage. The capacitor ESRs are also included.

## F.2 Include capacitor ESR to accurately measure high $Q$

For measuring high  $Q$ , the approximation made in [11] and [12] that the equivalent series resistances (ESRs) of the capacitors ( $R_{C_1}$ ,  $R_{C_2}$ ) are small compared to the equivalent series resistance of the inductor ( $R_L$ ) no longer holds, even with NP0, porcelain, or mica capacitors. For example, to measure an inductor with  $Q = 1000$ , using mica capacitors with  $Q = 4000$  would still introduce a 25% loss error in the measurement.

Since the capacitor ESRs are no longer negligible, we include them in deriving an expression for the quality factor of the inductor ( $Q_L$ ), using the measured input voltage  $v_{in}$  and stepped-down voltage  $v_{meas}$ . From Fig. F.1, we can see that at resonance, since the impedances of the inductor and capacitors cancel,

$$\frac{V_{meas,pk}}{V_{in,pk}} = \left| \frac{R_{C_2} + \frac{1}{j\omega_0 C_2}}{R_{C_1} + R_{C_2} + R_L} \right| \quad (\text{F.1})$$

We also know that at resonance,

$$Q_L = \frac{\omega_0 L}{R_L} \quad (\text{F.2})$$

From (F.1) and (F.2), the quality factor of the inductor as a function of  $V_{in,pk}$  and  $V_{meas,pk}$  is

$$Q_L = \frac{\omega_0 L}{\frac{V_{in,pk}}{V_{meas,pk}} \sqrt{R_{C_2}^2 + \left(\frac{1}{\omega_0 C_2}\right)^2} - R_{C_1} - R_{C_2}} \quad (\text{F.3})$$

where  $R_{C_1}$  and  $R_{C_2}$  are the ESR values found on the datasheet for the capacitors.<sup>1</sup>

The non-negligible capacitor ESR loss was validated thermally. At around 3 MHz, the highlighted mica capacitor in Fig. F.2 has an ESR of  $\sim 0.07 \Omega$ , as extrapolated from the datasheet. With 2.0 A of current and a thermal resistance of  $95 \text{ }^\circ\text{C}/\text{W}$  for the closest standard package size (2010) [42], we expect the capacitor to have a  $\sim 13 \text{ }^\circ\text{C}$  temperature rise, which agrees with the thermal image. This agreement confirms that the capacitor ESR loss can be predicted, and thus, corrected for when measuring the  $Q$  of the inductor.

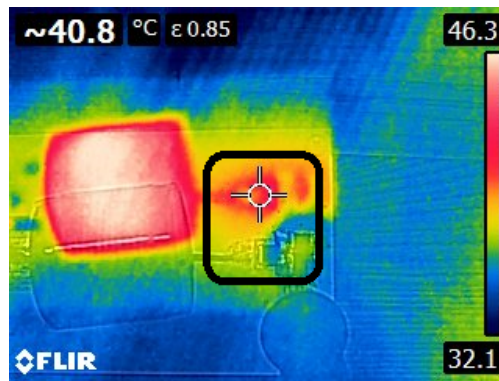


Figure F.2: Thermal image showing a mica capacitor (black box) with a  $\sim 13 \text{ }^\circ\text{C}$  temperature rise due to its ESR loss, in accordance with calculations.

<sup>1</sup>In cases where the capacitors are physically composed of multiple capacitors in parallel, the ESRs  $R_{C_1}$  and  $R_{C_2}$  can each be approximated as the equivalent parallel resistance for the corresponding ESRs.  $C_1$  and  $C_2$  can also be approximated as the equivalent parallel capacitance of the capacitors comprising it.

### F.3 Minimize dielectric loss through careful board layout

For measuring a high- $Q$  inductor, the node between the inductor and the capacitor divider sees a high voltage at HF. Therefore, in a layout where the return path runs directly under this high voltage node, the resulting parasitic capacitor can have non-negligible dielectric loss. We can mathematically show this by modeling the dielectric loss as the ESR loss of the parasitic capacitor. The dielectric loss is

$$P_{loss} = \frac{1}{2}V^2\omega C \tan \delta \quad (\text{F.4})$$

where  $V$  is the peak voltage at the node,  $\omega$  is the measurement frequency,  $C$  is the parasitic capacitance, and  $\tan \delta$  is the dielectric loss tangent of the board material.

As seen from (F.4), nodes with high voltages ( $\sim 1000$  V) can have substantial dielectric loss, especially when their parasitic capacitance and the dielectric loss tangent of the board are relatively large. For example, for measuring the  $Q$  of the example inductor (Fig. 3.2), the high voltage node expects  $\sim 600$  V at 3 MHz. If the node has an area of  $1 \text{ cm}^2$  on a standard 1.6 mm-thick FR-4 board ( $\tan \delta = 0.02$ ), the dielectric loss at this node is then 160 mW, which is about 20% of the inductor loss.

To minimize the dielectric loss, the capacitance at the high voltage node should be minimized by using a small node area and thick board. Board material with a lower dielectric loss tangent than FR-4, e.g. Rogers 4350B, can also be considered.

### F.4 Resonant measurement approach validated using an air-core inductor

We validated the large-signal measurement approach described above with small-signal  $Q$  measurements of an air-core inductor. Since an air-core inductor has no nonlinear core loss, its small-signal and large-signal quality factors are the same. Using the equivalent series resistance of an air-core inductor measured at 3 MHz (with an Agilent 4395A Impedance Analyzer and a custom resonant fixture), the small-signal quality factor of the inductor was calculated to be  $Q = 540$  at this frequency. Using the large-signal resonant measurement approach, the same air-core inductor had a measured quality factor of  $Q = 500$  at 3 MHz and 2 A (peak) of ac current, which validates this approach for measuring large-signal  $Q$  in this range. For even higher  $Q$  ( $>1000$ ), sources of error have a greater impact on measurements, which makes it more difficult to accurately measure  $Q$ . The validation of the air-core inductor at  $Q = 500$ , however, indicates that it is possible to accurately measure even higher  $Q$  using this measurement approach.

## Appendix G

### Constant Heat Flux Model

The constant heat flux model is a conservative model for predicting temperature rises in a magnetic structure. This model assumes that power is evenly dissipated over the entire surface area of the structure. Less conservative heat flux models exist, such as the empirical model in [36], but for simplicity, we chose to use the constant heat flux model. In this model [43], the power dissipated in a structure is proportional to the surface area of the structure and the temperature rise,

$$P \approx kA\Delta T \tag{G.1}$$

where  $k$  is the heat transfer coefficient.

We approximated  $k$  for the proposed structure, which is composed of Fair-Rite 67 core material, from thermal data in Fig. F.2. In the figure, the temperature of the inductor was roughly 46 °C. The inductor had a surface area of 3334 mm<sup>2</sup> and measured power loss of 0.702 W. Assuming the room temperature was 25 °C,

$$k \approx \frac{P}{A\Delta T} = \frac{0.702 \text{ W}}{3334 \text{ mm}^2(46 \text{ °C} - 25 \text{ °C})} = 10.03 \text{ W/m}^2\text{°C} \tag{G.2}$$

This value of  $k$  was then used to model the temperature rise for all simulations in Chapter 4.

## Appendix H

### Including Loss from Self-Resonant Circulating Currents in the Quality Factor

This section discusses how to incorporate the loss due to self-resonant circulating currents in the  $Q$  of a structure in simulation. To do this, we first extract the initial  $Q$  and the parasitic capacitance  $C_L$  of the structure from FEA simulation. Using this initial  $Q$ , we can model the core and copper losses of the inductor as a series resistance

$$R_L = \frac{\omega L}{Q} \quad (\text{H.1})$$

From there, we model the inductor as an ideal inductor with a series resistance and a parallel parasitic capacitor (Fig. H.1). To capture the circulating currents, we drive the inductor with a sinusoidal current source at the frequency and drive level of interest to get the total rms current flowing through the series resistance. We then calculate the expected total power loss and back out the quality factor accordingly as

$$Q = \frac{\pi f L I^2}{P_{diss}} = \frac{\pi f L I^2}{I_{R_L, rms}^2 R_L} \quad (\text{H.2})$$

where  $f$  is the frequency of interest,  $L$  is the inductance,  $I$  is the peak current of interest,  $I_{R_L, rms}$  is the total rms current flowing through the series resistance, and  $R_L$  is the series resistance.

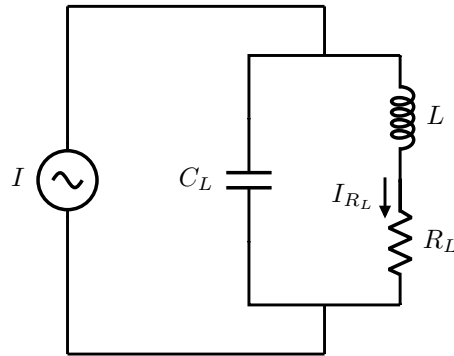


Figure H.1: Circuit for including loss from self-resonant circulating currents in the  $Q$  of an inductor. The non-idealities of the inductor are modeled with a series resistance for loss and a parallel parasitic capacitance. Using this circuit, the total rms current in the inductor is simulated and used to calculate the  $Q$ .

## Appendix I

### Example Python Script for Automating Initial Designs of the Modified Structure

```
#####  
# Example python script for automating the design process of the modified  
# inductor structure  
#  
# Authors: R. Bayliss III , R. S. Yang  
#  
# Notes:  
#   Compatibility with both Python 2 & 3  
#  
# Date last modified: 05.18.2019  
#####  
  
# libraries  
from __future__ import print_function # for compatibility with both Python 2 & 3  
import math  
  
u0 = 1.257e-6 # permeability of free space in [H/m]  
Fv = 0.6 # vertical fill factor of winding in window  
# (can range from 0 to 1, recommended range from 0.5 to 0.8)  
Fh = 1.0 # horizontal fill factor of winding in window  
# (can range from 0 to 1, recommended range from 0.4 to 0.6)  
ratio = 1.1 # aspect ratio (defined as height/diameter) (optimized at 1.0)  
  
# input variables  
uc = 40. # relative permeability of core material  
L = 500e-9 # desired inductance in [H]  
N = 2 # number of turns  
Ng = 10 # number of gaps  
h = 31.3e-3 # height of end cap [m]  
  
if __name__ == '__main__':  
  
    # compute fringing field reluctance Rf needed to achieve double-sided conduction for the  
    # desired L  
    Rf_min = N**2/(2*L)  
  
    # compute total radius rt based on fringing field reluctance approximation
```

```

# NOTE: here, we use Eq. 8 in the paper, which derives Rf from the air-core
# solenoid model found in:
#       T. H. Lee, Planar Microwave Engineering: A Practical Guide to Theory,
#       Measurement, and Circuits, 1st ed., Cambridge University Press, 2004,
#       pp. 140–142.
rt = .9*2*L / (N**2*u0*math.pi)

# compute total height ht using the computed total radius rt and the desired aspect
# ratio
ht = rt*2 / ratio

# compute wire diameter (Dw) to achieve desired vertical window fill (Fv)
Dw = (ht - 2.*h) * Fv / N

# compute window width (w) to achieve desired horizontal window fill (Fh)
w = Dw / Fh

# compute center post radius rc
rc = rt - w

# compute total gap length lg to match the center post and fringing field reluctances
lt = ht - 2.*h
lg = (0.9*rc**2*uc / rt - lt) / (uc - 1)

# compute the height of each center post core disc
lc = lt - lg
hdisc = lc / (Ng+1)

# compute length of each individual gap
lgs = lg / Ng

# compute center to center disc spacing
cc_disc = lgs + hdisc

# compute volume of structure
vol = math.pi*rt**2*ht

print("GEOMETRIC PARAMETERS FOR L = ", L, "H, volume = ", vol, "m^3")
print("Total height: ", round(ht*1000,3),"mm")
print("Total radius: ", round(rt*1000,3),"mm")
print("End cap height: ", round(h*1000,3),"mm")
print("Disc radius: ", round(rc*1000,3),"mm")
print("Disc height: ", round(hdisc*1000,3),"mm")
print("Individual gap length: ", round(lgs*1000,3),"mm")
print("Center to center disc spacing: ", round(cc_disc*1000,3), 'mm')
print("Ng: ", Ng)
print("WIRE SPECS: ")
print("Place wire center at x = ", round((Dw/2+rc+cc_disc/4)*1000,3), "mm & z = ", round
((h+(ht-2*h)/(N+1)) * 1000,3), "mm")
print("Wire radius: ", round(Dw/2*1000,3),"mm")
print("Center to center wire spacing: ", round((ht-2*h)/(N+1)*1000,3), "mm")

```

# Bibliography

- [1] F. E. Terman, *Radio Engineers' Handbook*, 1st ed. McGraw-Hill Book Company, Inc., 1943, pp. 52–55.
- [2] C. R. Sullivan, B. A. Reese, A. L. F. Stein, and P. A. Kyaw, “On size and magnetics: Why small efficient power inductors are rare,” in *2016 International Symposium on 3D Power Electronics Integration and Manufacturing (3D-PEIM)*, June 2016, pp. 1–23.
- [3] C. R. Sullivan, “Prospects for advances in power magnetics,” in *CIPS 2016; 9th International Conference on Integrated Power Electronics Systems*, March 2016, pp. 1–9.
- [4] P. A. Kyaw, A. L. F. Stein, and C. R. Sullivan, “High-q resonator with integrated capacitance for resonant power conversion,” in *2017 IEEE Applied Power Electronics Conference and Exposition (APEC)*, March 2017, pp. 2519–2526.
- [5] A. L. F. Stein, P. A. Kyaw, and C. R. Sullivan, “High-q self-resonant structure for wireless power transfer,” in *2017 IEEE Applied Power Electronics Conference and Exposition (APEC)*, March 2017, pp. 3723–3729.
- [6] C. R. Sullivan, “Aluminum windings and other strategies for high-frequency magnetics design in an era of high copper and energy costs,” in *APEC 07 - Twenty-Second Annual IEEE Applied Power Electronics Conference and Exposition*, Feb 2007, pp. 78–84.
- [7] J. Qiu, A. Hanson, and C. Sullivan, “Design of toroidal inductors with multiple parallel foil windings,” in *14th Workshop on Control and Modeling for Power Electronics (COMPEL)*. IEEE, 2013, pp. 23–26.
- [8] Y. Han and D. J. Perreault, “Inductor design methods with low-permeability rf core materials,” *IEEE Transactions on Industry Applications*, vol. 48, no. 5, pp. 1616–1627, Sept 2012.
- [9] J. Hu and C. R. Sullivan, “The quasi-distributed gap technique for planar inductors: design guidelines,” in *Industry Applications Conference, 1997. Thirty-Second IAS Annual Meeting, IAS '97., Conference Record of the 1997 IEEE*, vol. 2, Oct 1997, pp. 1147–1152 vol.2.
- [10] EPCOS AG – a TDK Group Company, “Distributed air gaps in ferrite cores,” June 2017. [Online]. Available: <https://de.tdk.eu/download/2113422/321697054fce0c768ea66959fde3b3db/ferrites-air-gaps-pb.pdf>
- [11] A. J. Hanson, J. A. Belk, S. Lim, C. R. Sullivan, and D. J. Perreault, “Measurements and performance factor comparisons of magnetic materials at high frequency,” *IEEE Transactions on Power Electronics*, vol. 31, no. 11, pp. 7909–7925, Nov 2016.
- [12] Y. Han, G. Cheung, A. Li, C. Sullivan, and D. Perreault, “Evaluation of magnetic materials for very high frequency applications,” *IEEE Transactions on Power Electronics*, pp. 425–435, 2008.
- [13] P. L. Dowell, “Effects of eddy currents in transformer windings,” *Electrical Engineers, Proceedings of the Institution of*, vol. 113, no. 8, pp. 1387–1394, August 1966.
- [14] C. R. Sullivan, “Optimal choice for number of strands in a litz-wire transformer winding,” *IEEE Transactions on Power Electronics*, vol. 14, no. 2, pp. 283–291, Mar 1999.
- [15] W. G. Hurley, E. Gath, and J. G. Breslin, “Optimizing the ac resistance of multilayer transformer windings with arbitrary current waveforms,” *IEEE Transactions on Power Electronics*, vol. 15, no. 2, pp. 369–376, Mar 2000.
- [16] T. Delaforge, H. Chazal, J. L. Schanen, and R. J. Pasterczyk, “Increasing windings efficiency at high frequencies: Hollow conductors and clad metal conductors formal solution based on the magnetic potential,” in *2015 IEEE Energy Conversion Congress and Exposition (ECCE)*, Sept 2015, pp. 5689–5695.
- [17] X. Nan and C. R. Sullivan, “An improved calculation of proximity-effect loss in high-frequency windings of round conductors,” in *Power Electronics Specialist Conference, 2003. PESC '03. 2003 IEEE 34th Annual*, vol. 2, June 2003, pp. 853–860 vol.2.
- [18] M. Chen, M. Araghchini, K. K. Afridi, J. H. Lang, C. R. Sullivan, and D. J. Perreault, “A systematic approach to modeling impedances and current distribution in planar magnetics,” *IEEE Transactions on Power Electronics*, vol. 31, no. 1, pp. 560–580, Jan 2016.



- 
- [19] K. Venkatachalam, C. R. Sullivan, T. Abdallah, and H. Tacca, "Accurate prediction of ferrite core loss with nonsinusoidal waveforms using only steinmetz parameters," in *2002 IEEE Workshop on Computers in Power Electronics, 2002. Proceedings.*, June 2002, pp. 36–41.
- [20] J. Muhlethaler, J. Biela, J. W. Kolar, and A. Ecklebe, "Improved core-loss calculation for magnetic components employed in power electronic systems," *IEEE Transactions on Power Electronics*, vol. 27, no. 2, pp. 964–973, Feb 2012.
- [21] C. Fei, F. C. Lee, and Q. Li, "High-efficiency high-power-density llc converter with an integrated planar matrix transformer for high output current applications," *IEEE Transactions on Industrial Electronics*, vol. PP, no. 99, pp. 2428–2435, 2017.
- [22] R. S. Yang, A. J. Hanson, D. J. Perreault, and C. R. Sullivan, "A low-loss inductor structure and design guidelines for high-frequency applications," in *2018 IEEE Applied Power Electronics Conference and Exposition (APEC)*, March 2018, pp. 579–586.
- [23] R. S. Yang, A. J. Hanson, B. A. Reese, C. R. Sullivan, and D. J. Perreault, "A low-loss inductor structure and design guidelines for high-frequency applications," *IEEE Transactions on Power Electronics*, pp. 1–1, 2019.
- [24] C. P. Steinmetz, "On the law of hysteresis," *Transactions of the American Institute of Electrical Engineers*, vol. IX, no. 1, pp. 1–64, Jan 1892.
- [25] J. G. Kassakian, M. F. Schlecht, and G. C. Verghese, *Principles of Power Electronics*. Pearson Education, Inc., 1991.
- [26] D. Neumayr, D. Bortis, J. W. Kolar, S. Hoffmann, and E. Hoene, "Origin and quantification of increased core loss in mnzn ferrite plates of a multi-gap inductor," *CPSS Transactions on Power Electronics and Applications*, vol. 4, no. 1, pp. 72–93, March 2019.
- [27] R. W. Erickson and D. Maksimovic, *Fundamentals of Power Electronics*, 2nd ed. Kluwer Academic Publishers, 2004.
- [28] T. H. Lee, *Planar Microwave Engineering: A Practical Guide to Theory, Measurement, and Circuits*, 1st ed. Cambridge University Press, 2004, pp. 140–142.
- [29] V. Valchev and A. Van den Bossche, *Inductors and Transformers for Power Electronics*. CRC Press, 2005.
- [30] J. W. Kolar, F. Krismer, M. Leibl, D. Neumayr, L. Schrittwieser, and D. Bortis, Impact of Magnetics on Power Electronics Converter Performance – State-of-the-Art and Future Prospects, Keynote Presentation at the PSMA Workshop on "Power Magnetics @ High Frequency – Transforming the Black Magic to Engineering", Tampa, FL, USA, March 25, 2017.
- [31] A. J. Hanson and D. J. Perreault, "A high frequency power factor correction converter with soft switching," in *IEEE Applied Power Electronics Conference (APEC)*, 2018.
- [32] C. R. Sullivan and R. Y. Zhang, "Simplified design method for litz wire," in *IEEE App. Pow. Electr. Conf. (APEC)*, 2014, pp. 2667–2674.
- [33] B. A. Reese, R. Joseph, and C. R. Sullivan, "Improved litz wire designs for the MHz range," in *2018 IEEE 19th Workshop on Control and Modeling for Power Electronics (COMPEL)*, June 2018.
- [34] J. D. Pollock, T. Abdallah, and C. R. Sullivan, "Easy-to-use CAD tools for litz-wire winding optimization," in *IEEE App. Pow. Electr. Conf.*, 2003.
- [35] C. R. Sullivan and R. Y. Zhang, "Analytical model for effects of twisting on litz-wire losses," in *IEEE Workshop on Control and Modeling for Pow. Electr. (COMPEL)*, 2014.
- [36] D. J. Perreault, J. Hu, J. M. Rivas, Y. Han, O. Leitermann, R. C. N. Pilawa-Podgurski, A. Sagneri, and C. R. Sullivan, "Opportunities and challenges in very high frequency power conversion," in *2009 Twenty-Fourth Annual IEEE Applied Power Electronics Conference and Exposition*, Feb 2009, pp. 1–14.
- [37] TDK, "Mn-zn ferrite cores for switching power supplies, rm series," May 2019. [Online]. Available: [https://product.tdk.com/info/en/catalog/datasheets/ferrite\\_mz\\_sw\\_rm\\_en.pdf](https://product.tdk.com/info/en/catalog/datasheets/ferrite_mz_sw_rm_en.pdf)
- [38] Magnetics, "Ferrite pot cores," May 2019. [Online]. Available: [https://product.tdk.com/info/en/catalog/datasheets/ferrite\\_mz\\_sw\\_rm\\_en.pdf](https://product.tdk.com/info/en/catalog/datasheets/ferrite_mz_sw_rm_en.pdf)
- [39] R. G. Medhurst, "H.f. resistance and self-capacitance of single-layer solenoids," *Wireless Engineer*, pp. 35–43, February 1947.
- [40] —, "H.f. resistance and self-capacitance of single-layer solenoids," *Wireless Engineer*, pp. 80–92, March 1947.
- [41] A. Massarini and M. K. Kazimierczuk, "Self-capacitance of inductors," *IEEE Transactions on Power Electronics*, vol. 12, no. 4, pp. 671–676, July 1997.

## Bibliography

---

- [42] Vishay, “Power dissipation in high precision Vishay Sfernice chip resistors and arrays (p thin film, p arrays, ctp thick film),” June 2018. [Online]. Available: <https://www.vishay.com/docs/53048/pprachp.pdf>
- [43] J. Hu, “Design of low-voltage, high-bandwidth radio frequency power converters,” Ph.D. dissertation, Massachusetts Institute of Technology, 2012.